

The NEWFIRM HETDEX Survey: Photometric Catalog and a Conservative Sample of Massive Quiescent Galaxies
at $z = 3 - 5$ over 17.5 deg^2 in the SHELA Field

MATTHEW L. STEVANS,¹ STEVEN L. FINKELSTEIN,¹ LALITWADEE KAWINWANICHAKIJ,^{2,3,4} ISAK WOLD,⁵ CASEY PAPOVICH,^{2,3}
RACHEL S. SOMERVILLE,^{6,7} L. Y. AARON YUNG,^{7,6} SYDNEY SHERMAN,⁸ ROBIN CIARDULLO,^{9,10} ROMEEL DAVÉ,¹¹
JONATHAN FLOREZ,⁸ CARYL GRONWALL,^{9,10} AND SHARDHA JOGEE⁸

¹*Department of Astronomy, University of Texas at Austin, Austin, TX 78712*

²*Department of Physics and Astronomy, Texas A&M University, College Station, TX, 77843-4242 USA*

³*George P. and Cynthia Woods Mitchell Institute for Fundamental Physics and Astronomy, Texas A&M University, College Station, TX, 77843-4242 USA*

⁴*LSSTC Data Science Fellow*

⁵*Astrophysics Science Division, Goddard Space Flight Center, 8800 Greenbelt Road, Greenbelt, Maryland, 20771*

⁶*Center for Computational Astrophysics, Flatiron Institute, 162 5th Avenue, New York, NY, 10010, USA*

⁷*Department of Physics and Astronomy, Rutgers, The State University of New Jersey, Piscataway, NJ, 08854, USA*

⁸*Department of Astronomy, University of Texas at Austin, Austin, TX 78705*

⁹*Department of Astronomy & Astrophysics, The Pennsylvania State University, University Park, PA 16802*

¹⁰*Institute for Gravitation and the Cosmos, The Pennsylvania State University, University Park, PA 16802*

¹¹*Institute for Astronomy, Royal Observatory, University of Edinburgh, Edinburgh EH9 3HJ, UK*

(Accepted March 23, 2021)

Submitted to ApJ

ABSTRACT

We present the results of a deep K_s -band ($2.1 \mu\text{m}$) imaging survey of the *Spitzer*/HETDEX Exploratory Large Area (SHELA) field using the NEWFIRM near-infrared (NIR) camera on the KPNO Mayall 4-m telescope. This NEWFIRM HETDEX Survey (NHS) reaches a 5σ depth of 22.4 AB mag ($2''$ -diameter apertures corrected to total), is $\sim 50\%$ and 90% complete at $K \sim 22.65$ and $K \sim 22.15$, respectively, and covers 22 deg^2 of the 24 deg^2 SHELA *Spitzer*/IRAC footprint (within “Stripe 82” of the Sloan Digital Sky Survey). We present a K_s -band-selected catalog which includes deep *ugriz* imaging from the Dark Energy Camera and 3.6 and $4.5 \mu\text{m}$ imaging from *Spitzer*/IRAC, with forced-photometry of 1.7 million sources across 17.5 deg^2 . The large area and moderate depth of this catalog enables the study of the most massive galaxies at high redshift, and minimizes uncertainties associated with counting statistics and cosmic variance. As a demonstration, we derive stellar masses (M_*) and star-formation rates (SFRs) for candidate galaxies at $3 \lesssim z \lesssim 5$, and select a conservative sample of nine candidate massive ($M_* > 10^{11} M_\odot$) quiescent galaxies, which have measured SFRs significantly below the main-sequence at this redshift. Five are ultra-massive with $M_* > 10^{12}$, though uncertainties in IRAC blending, gravitational lensing, or AGN emission could result in true masses which are lower. Simulations predict that these galaxies should be extremely rare, thus we conclude by discussing what physical processes in models could be altered to allow the formation of such massive quiescent galaxies at such early times.

Keywords: catalogs — infrared: galaxies — surveys

1. INTRODUCTION

It is well-established observationally that massive galaxies in the local Universe have a strongly bimodal color distribution (Baldry et al. 2004; Bell et al. 2004).

This is interpreted as indicating the presence of a star forming population of galaxies, which generally populate a relatively tight relation between stellar mass and star formation rate (SFR), and a population of “quiescent” galaxies that contain predominantly old stellar populations (Brinchmann et al. 2004). It is also well-established that the stellar mass and number of galaxies contained in this quiescent population has increased significantly over cosmic time since $z \sim 2$ (e.g., Kriek et al. 2006; Muzzin et al. 2013; Stefanon et al. 2013; Brennan et al. 2015), while the mass in the star forming population has remained nearly constant, indicating that some process (which has come to be commonly referred to as “quenching”) is causing star forming galaxies to stop forming new stars and become “red and dead”. The observed predominance of quiescent massive galaxies has historically been a challenge for theoretical models of galaxy formation, as the massive halos that host these objects are expected to experience rapid cooling flows of fresh gas to the center, where it should fuel star formation. Numerous physical mechanisms that could cause or contribute to quenching have been considered, but there is now a consensus that feedback processes related to radiation and kinetic energy injected by accreting supermassive black holes (AGN feedback) are likely the dominant mechanisms leading to long-lived quenching (see discussion in Somerville & Davé 2015, and references therein). Thus, constraining when the first quenched galaxies appeared in the Universe, and how common they are at early epochs, can provide critical constraints on when and where the first supermassive black holes formed, and how they impact their surroundings, which are key open questions in galaxy formation. Most recent simulations of galaxy formation are able to reproduce observed fractions of massive quenched galaxies in the local Universe (e.g., Kimm et al. 2009; Brennan et al. 2015; Nelson et al. 2018; Hahn et al. 2019), but reproducing as many massive quenched galaxies as observed at higher redshifts $z \gtrsim 2$ appears to pose a challenge for these models (Brennan et al. 2015; Merlin et al. 2019).

Such an investigation requires an unbiased census of massive galaxies over cosmic time. A number of observational studies have measured the number density of quiescent galaxies or the quiescent galaxy fraction out to high redshift (e.g., Dunlop et al. 2007; Marchesini et al. 2010; Muzzin et al. 2013; Straatman et al. 2014; Spitler et al. 2014; Brennan et al. 2015; Stefanon et al. 2015; Davidzon et al. 2017; Merlin et al. 2019), but the results differ substantially from one study to another. This may be in part because there is no clear universal definition of how to identify “true” qui-

escent galaxies at different epochs, but is likely also because these objects are quite rare, and these surveys have typically probed relatively small volumes, making counting statistics and field-to-field variance a substantial source of uncertainty. Additionally, there has been progress spectroscopically confirming massive quiescent galaxy candidates at $z > 3$ (e.g., Glazebrook et al. 2017; Schreiber et al. 2018; Tanaka et al. 2019; Forrest et al. 2020a; Valentino et al. 2020) and in ruling out obscured star formation with deep deep Atacama Large Millimeter/submillimeter Array (ALMA) observations (Santini et al. 2019), but more work is needed in both of these areas.

In this paper, we perform a systematic search for massive quiescent galaxies in the early universe ($3 < z < 5$) using deep multi-wavelength imaging across a wide area within the Spitzer/HETDEX Exploratory Large-Area (SHELA) field (Papovich et al. 2016). SHELA is a legacy field covering an area of $\sim 24 \text{ deg}^2$ within the footprints of the SDSS “Stripe 82” and the Hobby-Eberly Telescope Dark Energy Experiment (HETDEX; Hill & HETDEX Consortium 2016). HETDEX is measuring the effects of dark energy on the expansion rate of the universe via the baryonic acoustic oscillation (BAO) scale length by measuring spectroscopic redshifts of one million Lyman- α emitting galaxies at $z = 1.9 - 3.5$. The SHELA dataset includes deep (22.6 AB mag, 50% completeness) $3.6 \mu\text{m}$ and $4.5 \mu\text{m}$ imaging from Spitzer/IRAC (Papovich et al. 2016), $u'g'r'i'z'$ imaging from the Dark Energy Camera over 18 deg^2 (DECam; Wold et al. 2019), VISTA J and K_s photometry from the VICS82 survey (Geach et al. 2017), and a growing database of full-field IFU spectroscopy from HETDEX (presently $\sim 20\%$ complete).

Such a survey depends sensitively on the depth of its NIR imaging, and thus here we present the NEWFIRM HETDEX Survey¹ (NHS), a moderately deep K_s ($2.1 \mu\text{m}$) near-infrared (NIR) imaging survey with NEWFIRM on the KPNO Mayall 4m Telescope. The NHS adds to SHELA K_s -band imaging ($5\sigma K_s = 22.4 \text{ mag AB}$ in a $2''$ -diameter aperture) across 22 deg^2 , which is important for reducing the fraction of catastrophic errors in photometric redshifts and measuring robust star-formation rates (SFRs) by breaking the age-dust degeneracy. We present the NHS imaging and photometric catalog, along with a catalog of galaxy properties from SED-fitting for massive galaxies ($M/M_\odot > 10^{11}$) at $z = 3 - 5$. We highlight the utility of this catalog for exploring rare objects by identifying a conservative sam-

¹ NHS high-level image products will be available here: <https://www.noao.edu/survey-archives/>

ple of nine candidate massive galaxies ($M/M_{\odot} > 10^{11}$) which are quiescent (forming stars at a rate well below the main-sequence at that stellar mass).

This paper is organized as follows. The NHS observations and survey strategy are described in Section 2. The NHS data reduction, calibration, weighted combination, and position-dependent modeling of the point spread function (PSF) are described in Section 3. NHS source cataloging, including aperture photometry and error estimation, are described in Section 4. We describe the matching to the ancillary datasets (i.e., IRAC, DECam, and VICS82) in Section 5. Our method for deriving galaxy properties with `eazy-py` is described in Section 6. Our sample selection, contamination estimation, and measurement of the quiescent fraction are presented in Section 7. The implications of our results are discussed in Section 8. We summarize our work and discuss future work in Section 9. Throughout this paper we assume a Planck 2014 cosmology, with $H_0 = 67.8$ km s $^{-1}$ Mpc $^{-1}$, $\Omega_M = 0.307$ and $\Omega_{\Lambda} = 0.693$ (Planck Collaboration et al. 2014). All magnitudes given are in the AB system (Oke & Gunn 1983).

2. OBSERVATIONS AND SURVEY STRATEGY

We observed the SHELA Field with the Mayall 4m Telescope at Kitt Peak National Observatory using the NOAO Extremely Wide-Field Infrared Imager (NEWFIRM; Probst et al. 2004) instrument and K_s broadband filter. The NEWFIRM detector is comprised of four, 2048 x 2048 ORION InSb arrays with localized responsivity defects and a pixel scale of $0.4''/\text{pixel}$. The field of view is $27.6' \times 27.6'$ including a $35''$ wide cross-shaped gap between the four detectors. Images were taken over 93 nights in semesters 2014B, 2015B, 2016B, and 2017B under NOAO Survey Program #13B-0236 (PI: Finkelstein).

The field was observed in a pattern of 109 tiled pointings in four rows that maximizes the area of overlap with the existing SHELA DECam observations (Wold et al. 2019) as shown in Figure 1. Each tile is labeled with a letter (A-D) and a number (0-28). The letter indicates the row (row A having the highest declination and D the lowest), while the number indicates the relative position in right ascension starting at 1 for the lowest right ascension. The tiles overlap each other by about 1 arcmin. After the nominal exposure time was reached in the initially planned 99 pointings, 10 supplemental pointings were added to row D to fill in the gaps between the large circular DECam pointings where data do not overlap.

To reach the target depth of $K_s = 22.7$ mag across the field (in $2''$ apertures), an exposure time of 160 minutes per pointing was planned. Each exposure was 60

seconds in length, made up of 6 coadditions of 10 seconds. To minimize overheads and permit timely focus adjustments due to truss temperature changes, exposures were run in 5 batches of 32 60-second exposures by automated scripts. To bridge the cosmetic defects on and the gap between detectors, each exposure was taken after random dithering within a $1' \times 1'$ square.

The initial 99 pointings were observed for at least 160 minutes, with a median of 166 minutes of exposure time per pointing. We observed longer in some pointings (up to ~ 400 minutes) when the seeing was poor, which was either noticed in real time at the telescope or at the end of each year when the stacks did not achieving the nominal depth. The 10 supplemental pointings were observed for between 64 and 132 minutes with pairs of supplemental pointings overlapping by $\sim 60\%$ (to better overlap the DECam footprint). The median and standard deviation of the exposure time of non-supplemental pointings are 154 minutes and 45 minutes, respectively, and the distribution of the exposure times for all tiles is plotted in the right panel of Figure 4. Some frames were not usable and omitted due to poor seeing conditions.

3. IMAGE REDUCTION

3.1. Data Reduction and Calibration

The NEWFIRM exposures were processed by the NOAO NEWFIRM calibration pipeline (Swaters et al. 2009) and were downloaded from the NOAO Science Archive². A detailed description of the NEWFIRM calibration pipeline reduction procedure can be found in the NOAO Data Handbook on the NOAO website³. We provide a brief summary of the procedure here. The NEWFIRM images were initially calibrated using exposures taken during the observing runs. The main calibration steps included artifact flagging, dark correction, linearity correction, flat-fielding, and sky subtraction. Next, the images were astrometrically calibrated with 2MASS reference images. Finally, the frames were remapped to a grid where each pixel is a square with a side length of $0.4''$. The final data products included the remapped science images and their associated data quality maps (DQMs).

We inspected the quality and usefulness of every individual exposure with special attention given to the images flagged in the observers log as potentially flawed. Flawed images were removed because of artifacts provided by dew on the filter-housing window, elongated sources due to loss of the guide star or wind shake of

² <http://archive.noao.edu/>

³ <http://ast.noao.edu/data/docs>

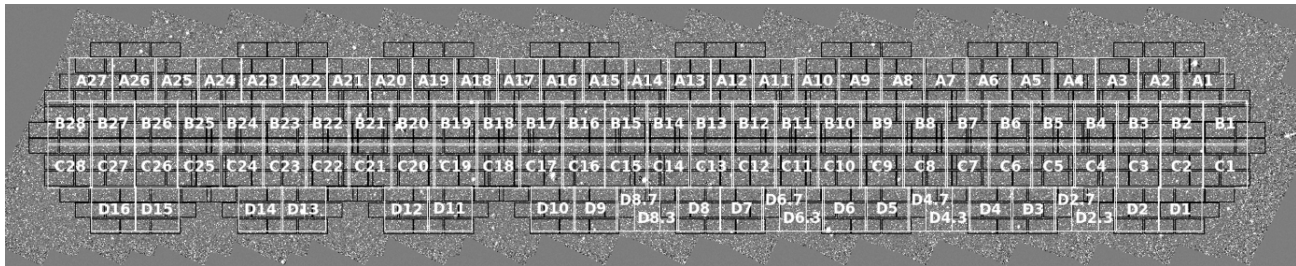


Figure 1. Layout of the NHS SHELTA field NEWFIRM pointings (white squares; $27.6' \times 27.6'$ field of view) overlaid on the IRAC data (grey) and the DECcam pointings (black; individual DECcam CCDs are traced). The left-most two (of eight) DECcam pointings were incomplete at the time of this analysis, thus are not used here. The NHS layout was designed to maximize the area of overlap with DECcam data. Ten additional overlapping NEWFIRM pointings were observed in row D after the nominal exposure time (160 minutes) was reached in the initially planned 99 pointings.

the telescope truss, triangular PSFs caused by loss of air pressure in the mirror supporting airbags, irregular structure in the background, and the erroneous masking of bright stars by the cosmic ray detection algorithm in the calibration pipeline.

During inspection, some pointings were found to have a number of exposures with corners exhibiting pixel values well above the typical background value. To avoid excluding the entire image, we flagged by eye all the pixels in the “bright corners” of a maximum-combined pointing image aligned in pixel-space and flagged those pixels in each affected image’s DQMs. This was repeated for each pointing as necessary. The pointings with masked “bright corners” include: A8, A11, A25, B17, C14, C16, D6, and D10.3.

3.2. Image Stacking

The remapped images that passed the visual inspection were combined using the PyRAF⁴ imcombine function and a weighted mean procedure optimized for point-sources. The weighting of each image is a function of the seeing, transparency, and sky brightness and is defined by Equation A3 in Gawiser et al. (2006) as

$$w_i^{\text{PS}} = \left(\frac{\text{factor}_i}{\text{scale}_i \times \text{rms}_i} \right)^2, \quad (1)$$

where scale_i is the image transparency (defined as the median brightness of the bright unsaturated stars after normalizing each star by its median brightness across all exposures), rms_i is the root mean square of the fluctuations of background pixels, and factor_i is defined as

$$\text{factor}_i = 1 - \exp \left(-1.3 \frac{\text{FWHM}_{\text{stack}}^2}{\text{FWHM}_i^2} \right), \quad (2)$$

where $\text{FWHM}_{\text{stack}}$ is the median full-width at half maximum (FWHM) of bright unsaturated stars in an un-

weighted stacked image and FWHM_i is the median FWHM of bright unsaturated stars in each individual exposure.

The seeing and transparency measurements were determined using a preliminary source catalog generated for each resampled image using the Source Extractor⁵ software package (Bertin & Arnouts 1996). The stars were selected from the stellar locus in the flux versus half-light radius parameter space and were required to appear in 80% of the exposures per pointing. The aperture used to measure the brightness was one that collects 99% of a star’s light as determined by the curve of growth technique. We quantified the noise in each exposure by calculating the standard deviation of flux measured in $2''$ -diameter apertures randomly positioned across the image. When doing this, we used only the negative side of the distribution to avoid biasing the measurement with signal from real sources.

To flux calibrate, we compared aperture-corrected NEWFIRM instrumental magnitude to the K_s -band magnitudes in the 2MASS catalog. The aperture-corrected NEWFIRM instrumental magnitude were extracted using an aperture enclosing 70% of the light from a point-source. This aperture size was determined using the curve of growth technique on a stacked image of 50 stars in the final image. To convert 2MASS Vega magnitudes to AB, we start with

$$m_X - m_{X,\text{ref}} = -2.5 \log \frac{\int d\nu T_X(\nu) S_\nu / h\nu}{\int d\nu T_X(\nu) S_\nu(\text{ref}) / h\nu}, \quad (3)$$

where $T_X(\nu)$ is the X filter transmission function and S_ν is the source function. When converting from Vega to AB the reference source function is a flat spectrum with $S_\nu(\text{ref})=3600$ Jy, such that

$$m_X = m_{AB} - 2.5 \log \frac{\int d\nu T_X(\nu) S_\nu / h\nu}{\int d\nu T_X(\nu) / h\nu}, \quad (4)$$

⁴ http://www.stsci.edu/institute/software_hardware/pyraf

⁵ Version 2.25.0; <https://www.astromatic.net/software/sextractor>

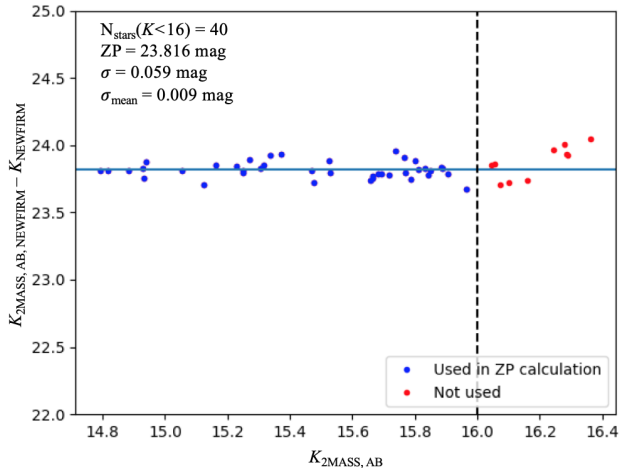


Figure 2. Zero-point offset between 2MASS K_s and NHS K_s for bright stars in stacked image tile D1. Each tile has many bright unsaturated stars that were used to determine the zero-point offset.

where

$$m_{AB} = -2.5 \log(3600 \text{ Jy}) = -48.61 \text{ mag} \quad (5)$$

when S_ν is in units of $\text{erg s}^{-1} \text{cm}^{-2} \text{Hz}^{-1}$. With $m_{X, Vega} \equiv 0$, the Vega to AB magnitude offset for 2MASS K_s is 1.8624 mag. To put the 2MASS K AB magnitudes into the NEWFIRM K_s magnitude system, we calculated the AB-Vega magnitude offset with the NEWFIRM K_s filter (1.8763 mag) and added the difference between that and the same quantity for the 2MASS K_s filter (0.0138 mag) to the 2MASS K_s AB magnitudes. This provided us with 2MASS measured magnitudes converted to both the AB system and the NEWFIRM K_s filter. The zeropoint offset was calculated as the sigma-clipped ($3\text{-}\sigma$, 2 iterations) average difference for a statistically robust sample ($N > 20$) of the brightest stars (typically $K_s < 16 - 17$ mag) selected from the stellar locus of the flux versus half-light radius plot per stacked image. The zeropoint magnitude calculated for tile D1 is shown in Figure 2 as an example.

The final NHS stacked images will be hosted on the NOAO Survey Archive⁶. As an example of our stacking process, in Figure 3 we show an individual image and the stack for tile B14. The distribution of stacked image qualities (seeing FWHM), $5\text{-}\sigma$ depths for $2''$ -diameter apertures, and the maximum exposure times are plotted in the three panels of Figure 4. The median (standard deviation) for all 109 tiles are $1.17''$ ($0.19''$), 22.78 mag (0.26 mag), and 154 minutes (45 minutes), respectively.

These $2''$ -diameter aperture $5\text{-}\sigma$ depths can be converted to the total depth for a point source by applying a median aperture correction of -0.35 mag.

3.3. Modeling Position-Dependent Point Spread Functions

The stacked images have non-uniform PSFs due to factors such as evolving seeing conditions and changes in telescope focus. However, within individual stacked images, the PSF varies smoothly as a function of position on the image. We modeled this behavior to obtain the most accurate aperture corrections, which allowed us to measure the highest-S/N fixed-aperture fluxes during the source cataloging procedure described in Section 4.

We modeled the spatially variable PSF in each stacked image using the PSF Extractor⁷ (PSFEx) software package (Bertin 2011). This software is well documented and we follow the default procedure described in the documentation which we summarize here.

The software takes a catalog from Source Extractor that includes the following for each detection: a small sub-image or “vignette,” centroid coordinate, half-light radius, signal-to-noise ratio in a Gaussian window, flux measured through a fixed aperture, flux uncertainty, object elongation, and extraction flags. Before running Source Extractor to create the input catalog, an rms image for each stacked image was needed for Source Extractor to generate reasonable flux uncertainties. We created this using the stacked science, DQM, and exposure time map images. The rms image was the inverse square of the exposure time map with the values scaled such that the median value of the resulting rms map equaled the sigma-clipped ($3\text{-}\sigma$, 2 iterations) standard deviation of pixel values in the science image where the exposure time is equal to the median and pixels contain no flux from objects. Objects are located using a segmentation map from a preliminary run of Source Extractor on each stacked image.

The PSFEx input catalog was created by running Source Extractor on each stacked image twice. The first run determined the pixel saturation level by finding the maximum pixel value of the brightest unsaturated star. The brightest unsaturated star was visually selected from the stellar locus on the flux versus half-light radius plot. We then set the gain and SATUR_LEVEL keywords to produce the binary fits catalog to be passed to PSFEx. The image gain was calculated as the average exposure time per pixel multiplied by the instrumental gain (8 electrons per ADU). The vignette size was set to 45 pixels by 45 pixels and the follow-

⁶ <https://www.noao.edu/survey-archives/>

⁷ Version 3.18.2; <http://www.astromatic.net/software/psfex>

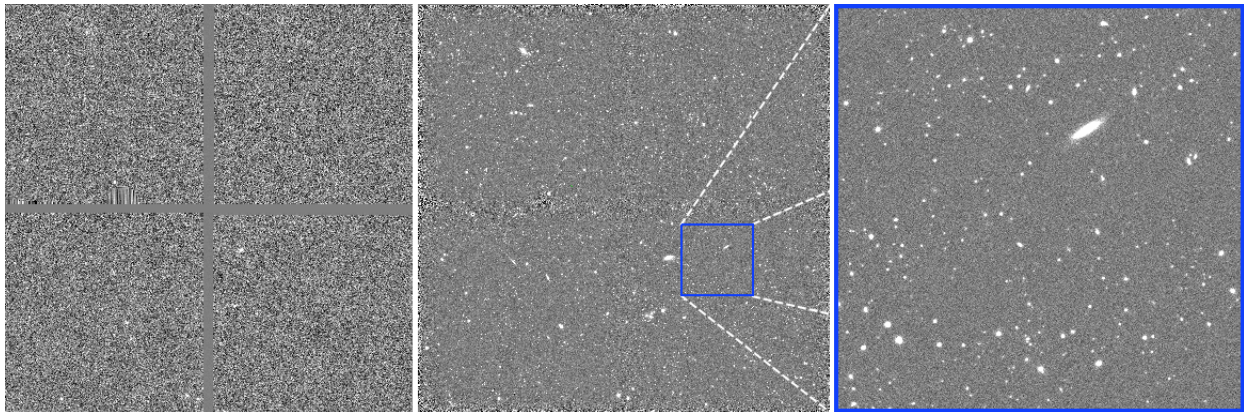


Figure 3. Left: A single one-minute NEWFIRM exposure of tile B14 in the NHS. Center: The stacked image of tile B14. Right: Zoom-in $\sim 5' \times \sim 5'$ cutout of tile B14 stacked image. The stacked images are a combination of dithered single exposures and therefore have relatively smooth backgrounds, with data filling the cross-shaped detector gap seen in the single exposure. Each field overlaps neighboring tiles by at least $1'$.

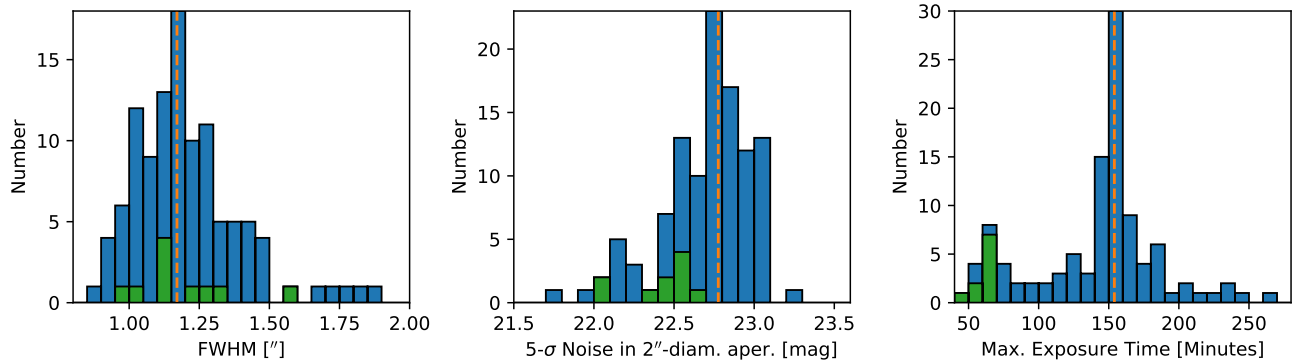


Figure 4. The median FWHM or seeing (left), $5\text{-}\sigma$ sky noise in $\sim 2''$ -diameter apertures as derived in Section 3.2 (center), and maximum exposure time (right) for each NHS tile (blue). The distribution of the 10 supplemental tiles are highlighted in green. The median of each distribution is plotted as a vertical orange dashed line. The $5\text{-}\sigma$ sky noise in $2''$ -diameter apertures for all fields relate to the $5\text{-}\sigma$ depths for total fluxes by an added median aperture correction of -0.35 mag and a standard deviation of 0.12 mag, and these values are within $\lesssim 0.1$ mag of those derived via the error functions in §4.2.

ing keywords were set to the values in the parentheses for this exercise: `DETECT_MINAREA` (6), `DETECT_THRESH` (1.3), `ANALYSIS_THRESH` (1.3), `DEBLEND_NTHRESH` (32), `DEBLEND_MINCONT` (0.005), `CLEAN` (Y), and `CLEAN_PARAM` (1.0).

Finally, we ran `PSFEx` on each stacked image with `BASIS_TYPE = PIXEL` which models the PSF in pixel space as a linear combination of a limited number of known basis functions. We use `BASIS_NUMBER = 31`, indicating only the central 31 pixel by 31 pixel region of each source vignette was used in the modeling. A 30-pixel-diameter aperture was used for normalizing the amplitude of the PSF model. We ran `PSFEx` with a range of polynomials ($n=2-8$) and found the order at which the χ^2 goodness of fit was minimized for each stacked image independently. We list the non-default parameter values used in the `PSFEx` runs in Table 1. These PSF

Table 1. Non-default `PSFEx` configuration parameters used

Parameter	Value
<code>BASIS_TYPE</code>	<code>PIXEL</code>
<code>BASIS_NUMBER</code>	31
<code>PSF_SAMPLING</code>	1
<code>PSF_SIZE</code>	31,31

models are used below to determine aperture corrections for fixed-aperture photometry.

4. NHS SOURCE CATALOG

Table 2. Relevant Source Extractor configuration parameters used

Parameter	Value
DETECT_MINAREA	5
DETECT_THRESH	1.0
ANALYSIS_THRESH	1.0
DEBLEND_NTHRESH	32
DEBLEND_MINCONT	0.005
CLEAN	Y
CLEAN_PARAM	1.0
BACK_SIZE	64
BACK_FILTERSIZE	3

We detected and extracted sources by running `Source Extractor`⁸ on each NEWFIRM K_s tile in one image mode with default `Source Extractor` parameters. The values of important or non-default `Source Extractor` parameters used are listed in Table 2. We selected the optimal values of `Source Extractor` parameters `DETECT_THRESH` and `MINAREA` by considering the recovery fraction of simulated sources injected into the stacked images and the false positive fraction. This process is described in Section 4.1. The source flux errors were estimated empirically (Section 4.2) and were used to find the aperture size that maximizes the S/N in each stacked image. Aperture corrections for the optimal apertures were determined using the position dependent PSF models (Section 4.3). Because the stacked images overlap on the sky, we combined the fluxes of sources in the overlap regions with a weighted mean in our final catalog (Section 4.5).

4.1. Deriving Source Selection Parameters

We selected the optimal values of `Source Extractor` parameters `DETECT_THRESH` and `MINAREA` for our stacked images by injecting mock point-sources into our images and calculating the fraction that were recovered by `Source Extractor`. We inserted 50,000 mock point-sources into each stacked image using the modeled PSF from `PSFEx` (Section 3.3) at random positions (excluding locations inside the isophotes of bright objects by a conservative amount). Mock sources were assigned magnitudes chosen randomly from a lognormal distribution in the range $K_s = 14.75$ –24.5 mag.

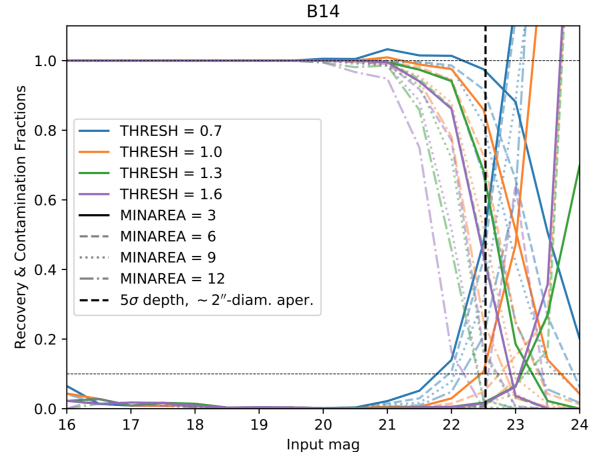


Figure 5. Recovery and false-positive (or contamination) fractions for various combinations of `Source Extractor` selection parameters (see legend) in tile B14. The recovery fraction can be greater than 1.0 due to spurious sources. We selected the combination that had a false-positive fraction below 10% and a recovery fraction above 50% in the faintest magnitude bin for most of the stacked images. The selected combination was `DETECT_THRESH = 1.0` and `MINAREA = 5`. We used these parameter values for all stacked images for consistency.

The recovery fraction of each magnitude bin was calculated as the number of mock sources recovered divided by the total number of mock sources injected. The false positive fraction per magnitude bin was calculated by multiplying the image by -1 , re-running `Source Extractor`, and dividing the number of sources detected in this inverted image (which are all noise spikes) by the number of sources in the original stacked image.

The recovery and false-positive fractions were calculated from a number of `Source Extractor` catalogs generated using combinations of `DETECT_THRESH` and `MINAREA` in the range 0.7–1.6 and 3–12, respectively. Figure 5 shows the recovery and false positive fractions for field B14. We selected the combination of parameters that produced a false-positive fraction below 10% and a recovery fraction above 50% in the faintest magnitude bin for most of the stacked images. This analysis led to the final selected combination of `DETECT_THRESH = 1.0` and `MINAREA = 5`, which we used for all stacked images.

4.2. Error Estimates

We estimated photometric uncertainties in the stacked images by fitting the image noise in apertures as a function of pixels per aperture, N , following the procedure described in Section 2.4 of [Stevans et al. \(2018\)](#) and based on the procedure of [Papovich et al. \(2016\)](#) (see

⁸ Version 2.25.0; <https://www.astromatic.net/software/sextractor>

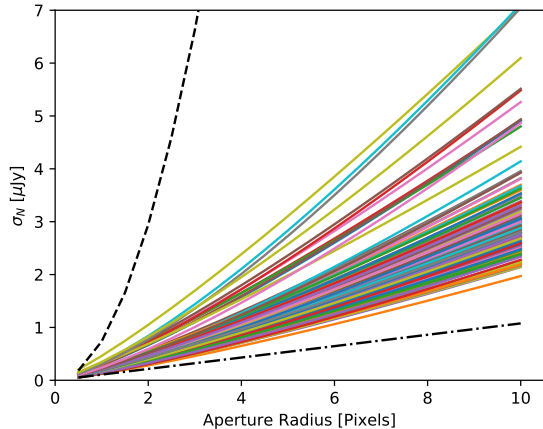


Figure 6. Parameterized fits to the background noise fluctuations, σ_N , in an aperture of N pixels plotted as a function of the aperture radius (in pixels) for all NHS tiles (colored lines). The dot-dashed black line shows the relation assuming uncorrelated pixels, $\sigma_N \sim \sqrt{N}$, for the tile with the largest σ_1 . The dashed black line shows the relation assuming perfectly correlated pixels, $\sigma_N \sim N$, for the tile with the smallest σ_1 (Quadri et al. 2007). Our fits are in the partially correlated regime. We use these parameterized fits to estimate source flux uncertainties in the NHS catalog.

also Labbé et al. 2002; Gawiser et al. 2006; Quadri et al. 2007; Whitaker et al. 2011). Our procedure differs in the following ways. We randomly positioned 50,000 non-overlapping, circular apertures on unflagged pixels absent of source flux (i.e., avoiding source footprints in the segmentation maps from `Source Extractor`). We fit a parameterized function to the noise in an aperture of N pixels, σ_N , with only two free parameters as,

$$\sigma_N = \sigma_1 \alpha N^\beta \quad (6)$$

where σ_1 is the pixel-to-pixel standard deviation in the sky background, and α and β are free parameters. The parameterized fits to the background noise fluctuations functions are shown in Figure 6.

4.3. Optimal-Aperture Sizes for Aperture Photometry of Point-Sources

After measuring each stacked image’s unique noise properties, we found the optimal-aperture size for each stacked image by finding the aperture size that maximized the S/N for point-sources. We plotted the aperture S/N as a function of aperture size for sources in each magnitude bin, noted the aperture size with the highest S/N, and selected the modal value giving a single optimal-aperture size per field. The median optimal-aperture diameter of all stacked images was $1.3''$ with a standard deviation of $0.20''$. The distribution of optimal-aperture diameter is plotted in Figure 7. We

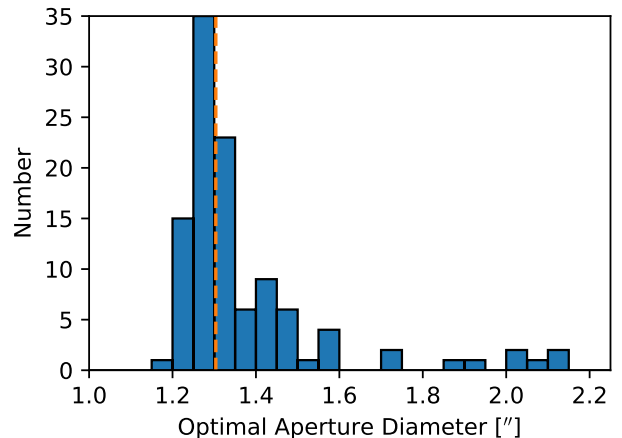


Figure 7. Distribution of optimal-aperture diameters for all NHS stacked tiles. The median optimal-aperture diameter was $1.3''$ with a standard deviation of $0.20''$. These apertures produce the highest S/N flux measurements for point-sources.

used the PSF model to calculate the localized aperture corrections for the optimal-aperture size of each stacked image on a per-object basis. The aperture corrections were calculated using the curve of growth technique on the model PSFs (Section 3.3) at 64 evenly spaced positions in a square grid across each tile.

4.4. AUTO Fluxes

Any photometric measurement made using the optimal aperture, even after correcting to total, is appropriate only for a point source. As the user of this catalog may be interested in resolved galaxies, we also include the Source Extractor “AUTO” flux. This flux is measured in an elliptical Kron aperture, where we use the default parameters which are tuned to recover approximately the total flux. We calculate uncertainties on these fluxes using the error functions derived in §4.2 and the area covered by these elliptical apertures (calculated for each source using the Source Extractor returned `A_IMAGE`, `B_IMAGE` and `KRON_RADIUS` values). Both the fluxes and uncertainties are corrected to total using an aperture correction of $1/0.94$, as the Source Extractor documentation shows that the default `MAG_AUTO` apertures typically contain 94% of the total flux.

4.5. Combining Catalogs of Overlapping Stacked Images

Since the stacked images overlap their neighboring tiles by $1-2'$ on all sides, some sources will appear in 2-4 stacked images and their respective catalogs. We combined duplicate sources for the final catalog. Any

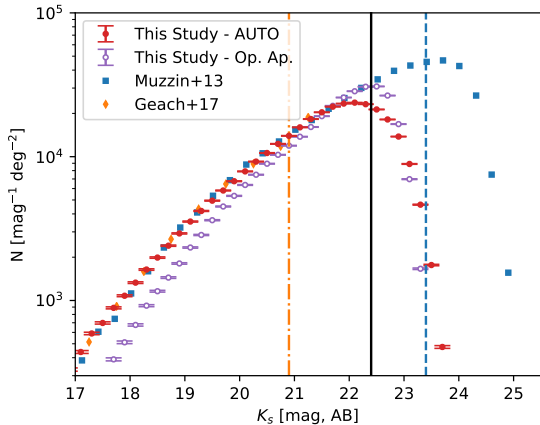


Figure 8. The NHS K_s -band galaxy differential number counts (with Poisson error bars) compared to those measured in the deeper near-infrared survey UltraVISTA (Muzzin et al. 2013) and the wider near-infrared survey VICS82 (Geach et al. 2017) (see legend). We include number counts derived using both `Source Extractor` AUTO apertures (filled purple circles) and from optimal apertures corrected to total (open red circles; see Section 4.3). The NHS data have not been corrected for incompleteness. The $5\text{-}\sigma$ depth derived from $2''$ -diameter aperture measurements, corrected to total ($K_s = 22.4$ mag, after a -0.35 mag aperture correction), is plotted as the black solid line. Number counts from the literature are reproduced from the published figures and the reported $5\text{-}\sigma$ limits from UltraVISTA and VICS82 are shown as the dashed and dot-dashed lines, respectively. Comparing to the deeper UltraVISTA catalog, we find that the NHS number counts are 90% complete at 22.0 (22.5) mag for AUTO (corrected optimal) apertures. Brighter than this, the NHS galaxy AUTO number counts agree well with both UltraVISTA and VICS82, while the corrected optimal circular apertures show a progressively larger shift towards fainter magnitudes as those apertures assume a point-source profile when correcting to total (while such bright sources will predominantly be resolved).

source within $0.6''$ of a source in another catalog was combined with each entry weighted by the inverse of its squared empirical error.

4.6. Number Counts

We compare the number counts of galaxies in our K_s -band NHS catalog using both `Source Extractor` AUTO (apertures and optimally sized apertures (both corrected-to-total) to values from the literature in Figure 8. This figure uses the final combined catalog, and thus effectively averages over differences in data quality between fields. Galaxies are defined as sources with a `Source Extractor` CLASS_STAR value of less than 0.95. Number counts from the literature are extracted from the published figures. We find our number counts to be in excellent agreement with the deeper near-infrared sur-

vey UltraVISTA (McCracken et al. 2012) which covers 1.6 deg^2 to a depth of 23.8 mag (Muzzin et al. 2013). Our number counts are also consistent with the number counts from the VICS82 survey (Geach et al. 2017) which covers $\sim 150 \text{ deg}^2$ to a depth of 20.9 mag. This figure shows that our K -band selected catalog is $\gtrsim 90\%$ complete at $K \sim 22.0$, and $\sim 70\%$ complete at our 5σ limit of 22.4.

5. MATCHING TO ANCILLARY DATASETS

5.1. IRAC Data Reduction and Photometry

In this subsection we discuss the photometric measurements of the SHELA *Spitzer*/IRAC imaging in this field. Full details of this dataset are available in Papovich et al. (2016), who find these data to be 50% complete to a limiting magnitude of 22.6 at both 3.6 and $4.5 \mu\text{m}$. To include these data in our catalog, we could position-match the published *Spitzer*/IRAC catalog from Papovich et al. (2016) to our NEWFIRM catalog, though this is not optimal for two reasons. First, the Papovich et al. (2016) catalog is IRAC-detected, and so only includes sources with significant IRAC flux. For our purposes, even a non-detection in IRAC can be useful for calculating a photometric redshift. Second, this catalog uses apertures defined by the positions and shapes of the IRAC sources. This is a significant limitation since the larger PSF of the IRAC data results in significant blending, especially at fainter magnitudes, where we expect to find the bulk of our high- z sources. For these reasons, we apply the `Tractor` image modeling code (Lang et al. 2016a,b) to perform “forced photometry,” which employs prior measurements of source positions and surface brightness profiles from a high-resolution band to model and fit the fluxes of the source in the remaining bands, splitting the flux in overlapping objects into their respective sources. We specifically use `Tractor` to optimize the likelihood for the photometric properties of NEWFIRM K_s -band sources in each of the IRAC 3.6 and $4.5 \mu\text{m}$ bands given initial information on the source and image parameters. The input parameters of the IRAC 3.6 and $4.5 \mu\text{m}$ images include a noise model, a PSF model, image astrometric calibration described by World Coordinate System (WCS), and calibration information (the “sky noise” or rms of the image background). The input source parameters include the NEWFIRM source positions, brightness, and surface brightness profile (i.e., effective radius, position angle, and axis ratio). `Tractor` then renders a model of a galaxy or a point-source, convolves it with the PSF model for each IRAC band, and performs a linear least-squares fit for source fluxes such that the sum of source

fluxes is closest to the actual image pixels, with respect to the noise model.

We model the surface brightness profile of NEWFIRM K_s -band sources using the same method as implemented in Wold et al. (2019) for the IRAC forced photometry of DECam-selected sources. We refer the reader to Wold et al. for the full description of surface brightness profile modeling (Section 4.2) and the photometric error estimates (Section 4.3). Here we briefly summarize how we use **Tractor** to perform forced photometry on IRAC images for NEWFIRM K_s -band-selected sources below.

We begin with using the fluxes and surface brightness profile shape parameters measured in our NEWFIRM K_s -band image as our initial high-resolution model. We then use an empirical IRAC point-response functions (PRFs) for the 3.6 and 4.5 μm images (FWHM of $1''.97$ and $1''.99$ from Gaussian fits to the 3.6 and 4.5 μm PRFs, respectively) to model each source. The construction of the IRAC PRF is described in Papovich et al. (2016) (Section 3.4). As in Wold et al. (2019), we apply the scaling factor of 0.265 and 0.287 to 3.6 and 4.5 μm weighted images, respectively, to generate the rms maps for **Tractor** forced photometry procedure. These rms maps result in the median photometric error output from **Tractor** roughly matched with those measured in $6''$ -diameter apertures, corrected to total, obtained from the published *Spitzer*/IRAC catalog (Papovich et al. 2016). For each NEWFIRM source, we extract an IRAC image cutout ($20'' \times 20''$) and measure its IRAC fluxes with three brightness profiles: a point-source profile, an exponential profile (equivalent to a Sérsic profile with $n = 1$), and deVaucouleurs profile (equivalent to a Sérsic profile with $n = 4$). The **Tractor** simultaneously modeled and optimized the sources of interest and neighboring sources within the cutout. Finally, the **Tractor** measured the IRAC flux of each NEWFIRM source with the lowest reduced chi-squared value, χ_{red}^2 . In our final output catalog of IRAC forced photometry, we use IRAC fluxes based on the optimized model profile (those with the lowest χ_{red}^2 among the three brightness profiles).

We validated the **Tractor**-based IRAC fluxes by comparing the fluxes of isolated sources (no neighbors within $4''$) to the published *Spitzer*/IRAC catalog from Papovich et al. (2016). For both bands, we find good agreement with an offset of $\delta m = 0.05$ mag and a scatter of 0.15 mag down to $m = 22$ mag.

5.2. DECam Photometry

In addition to performing NEWFIRM-based forced photometry on the IRAC images, we also used **Tractor** to optimize the likelihood for the photometric properties of NEWFIRM K_s -band sources in all five DECam

ugriz bands. The full details of these data are available in Wold et al. (2019), which finds a typical image quality of $\sim 1.5''$, and typical 5σ limiting magnitudes of $u \sim 25.4$, $g \sim 25.1$, $r \sim 24.6$, $i \sim 24.0$ and $z \sim 23.7$ from their PSF-matched data (see their Table 3 for full details). The input image parameters of the *ugriz* images include the empirical DECam PSFs, astrometric calibration, and sky noise for the stacked DECam images from Wold et al. (2019). We apply scaling factors to the DECam weighted images in each band and tile them to generate the rms map for the **Tractor** forced photometry procedure. We then used the same method as described in Section 5.1 and Wold et al. (2019) to model the brightness profile and estimate photometric errors for all sources. In our final output catalog of DECam forced photometry, we quote DECam fluxes based on the optimized model profile.

We validate the **Tractor**-based DECam fluxes by comparing the fluxes of isolated sources (no neighbors within $4''$) to the published *ugriz*-band DECam catalogs for the *Spitzer*/SHELA survey (Wold et al. 2019). For u' , g' , r' , i' , and z' bands, we find good agreement with a median bias offset of $\delta m = [0.04, 0.03, 0.06, 0.05, 0.04]$ mag and a scatter of $[0.14, 0.13, 0.11, 0.09, 0.10]$ mag, respectively, down to $m = 26$ mag (see Wold et al. 2019, for the FWHMs from Gaussian fits to the five *ugriz*-bands and four tiles).

5.3. Position-matching to VICS82

The VISTA-CFHT Stripe 82 Near-infrared Survey⁹ (VICS82; Geach et al. 2017) covers $\sim 85\%$ of the optical imaging footprint of our field with $J = 21.3$ mag and $K_s = 20.9$ mag imaging. The J -band data adds a missing wavelength to our catalog, and the K_s -band photometry, while ~ 2 magnitudes shallower than our NHS data, adds an independent measurement. We position-matched our source catalog to the publicly available February 2017 version of the VICS82 catalog (Geach et al. 2017). The matching radius used was $1.2''$.

On inspection of the magnitude difference between VICS82 K_s and 2MASS K_s and between VICS82 K_s and our NEWFIRM K_s (Figure 9; left panel), we found a locus of sources with Δmag offsets ~ 0.3 - 3 mag (green markers). A similar feature was found when comparing the VICS82 J source magnitudes to that of 2MASS J . We inspected the VICS82 science and weight map images at the position of some of the offset sources and found weight map pixel values of zero near the object centers, which led to underestimated fluxes. We flagged and removed any VICS82 flux measurements where the

⁹ <http://stri-cluster.herts.ac.uk/vics82/>

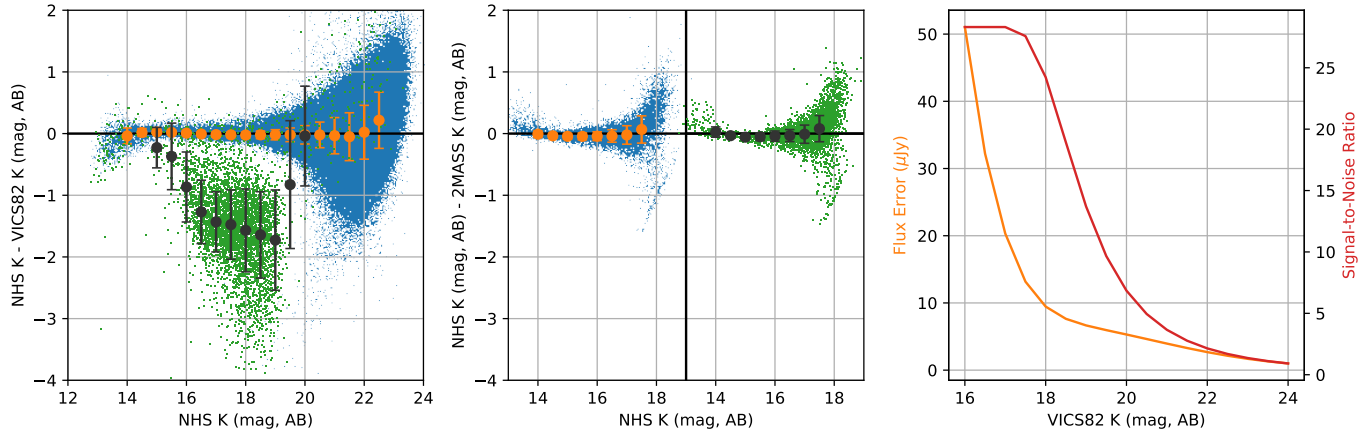


Figure 9. Left: Magnitude difference between NHS NEWFIRM K_s and VICS82 K_s filters for point-sources (blue) with the binned sigma-clipped median and standard deviations (orange). A locus of sources with significant offsets is seen (green) along with their binned sigma-clipped median and standard deviations (black). A similar locus is seen when comparing VICS82 J to 2MASS J . Center: Magnitude difference between NHS NEWFIRM K_s and 2MASS K_s filters for the same sources shown in the left panel plotted (when detected in 2MASS). The sources in the offset locus in the left panel show no offset between NEWFIRM K_s and 2MASS K_s . No filter offsets were applied in these figures. In our catalog, we flagged VICS82 fluxes of sources in the offset locus by identifying objects with weight map values of zero within the central 3x3 pixels. Values from these objects are not included in our catalog. Right: Our derived flux errors assigned to VICS82 J and K_s fluxes as a function of magnitude (orange line) along with the resulting signal-to-noise ratio (red line). The resulting 5- σ depths, $J = K_s = 20.75$ mag, are consistent with the depths reported for the VICS82 catalog ($J = 21.3$ mag and $K_s = 20.9$ mag) in Geach et al. (2017).

minimum weight-map pixel value within the 3 x 3 pixels of object centers is zero in either J or K_s . This resulted in the removal of 1% of VICS82 sources with NHS counterparts.

The February 2017 version of the VICS82 catalog contained no source error estimates. An indirect error estimate was contained in the Gaussian-weighted S/N column, but these errors are inappropriate for aperture photometry. To estimate the uncertainties of VICS82 flux measurements we assigned errors based on the standard deviation of the difference between VICS82 and NHS magnitudes as a function of VICS82 K_s magnitudes. We fitted the standard deviation from $K_s = 17$ -21.5 mag using the function $\alpha \cdot \text{STDDEV}^\beta$, where α and β are free parameters, after normalizing by the standard deviation in the mag=17 bin. For the J band, we adopted the K_s -band error function because we did not have an independent J -band catalog of sufficient depth. The VICS82 catalog states that the J -band images are deeper than K_s , so our J errors are conservatively large. The right panel of Figure 9 shows the estimated flux errors assigned to the VICS82 J and K_s fluxes as a function of magnitude along with the resulting signal-to-noise ratio. The 5- σ depths are $J = K_s = 20.75$ mag, which are similar to the 5- σ depths reported for the VICS82 catalog for K_s (20.9), and lower for J (21.3).

We note that although we have used multiple photometric techniques (Source Extractor for K_s , Tractor for DECam and IRAC, and the VICS82 published catalog),

we have strong evidence that there is no systematic bias in the measured photometry due to these specific techniques. For DECam and IRAC we find excellent agreement with previously published Source Extractor catalogs by Wold et al. (2019) and Papovich et al. (2016), respectively, and with VICS82, with the exception of the small number of outliers, we see excellent agreement with our own K_s -band photometry. One final piece of evidence comes from Sherman et al. (2020a), who used our catalog and derived photometric offsets calculated by finding the best-fit template for a set of galaxies with known spectroscopic redshifts with EAZY-py. They measured the median offsets between those template fluxes and the measured fluxes, finding a maximum offset of $\pm 2\%$, with $< 1\%$ in the majority of filters.

5.4. Correcting Photometry for Galactic Extinction

All source fluxes and errors were corrected for Galactic extinction using the color excess $E(B - V)$ measurements by Schlafly & Finkbeiner (2011). We obtained $E(B - V)$ values using the Galactic Dust Reddening and Extinction application on the NASA/IPAC Infrared Science Archive (IRAS) website¹⁰. We queried IRAS for $E(B - V)$ values (i.e., the mean value within a 5' radius) for a grid of points across the SHELA field. The grid had 120 values in right ascension ranging from 13°-25° and

¹⁰ <http://irsa.ipac.caltech.edu/applications/DUST/>

50 values in declination ranging from $-1^{\circ}25$ to $1^{\circ}25$. The median $E(B - V)$ was 0.0269 ± 0.007 (the minimum and maximum were 0.0159 and 0.1004, respectively). The $E(B - V)$ value of the grid point closest to each source was assigned. The [Cardelli et al. \(1989\)](#) Milky Way reddening curve parameterized by $R_V = 3.1$ was used to derive the corrections at each band’s central wavelength.

6. GALAXY PROPERTIES FROM EAZY-PY

We measured photometric redshifts and galaxy physical properties (e.g., stellar mass, star formation rate, rest-frame colors) by running the full NHS photometry catalog including ancillary data (Section 5) through the publicly available software package `eazy-py`¹¹ which is based on the EAZY code ([Brammer et al. 2008](#)). `eazy-py` finds the linear combination of 12 Flexible Stellar Population Synthesis (FSPS) templates ([Conroy et al. 2009](#); [Conroy & Gunn 2010](#)) that minimizes the χ^2 with respect to the extinction-corrected fluxes in all available photometric bands (i.e., DECam, NEWFIRM, VISTA and IRAC). For the remainder of our analysis, we used the Kron-based NEWFIRM flux from `Source Extractor` (e.g., `FLUX_AUTO`) corrected to total, such that these results should be appropriate even for resolved sources. Fluxes in all other bands also represent total fluxes, as described above.

The non-default configuration parameters we used to run `eazy-py` are listed in Table 3. We ran `eazy-py` with flat priors because we are exploring a volume and parameter space larger than existing surveys and simulations, which are often used to derive priors and can suffer from large uncertainties due to small number statistics and cosmic variance especially at the bright end of the luminosity function. This could bias redshift solutions for real high redshift massive galaxies in our survey towards lower redshifts. We used the recommended set of templates from ‘`templates/fsps_full/tweak_fsps.QSF_12.v3.param`’ (G. Brammer, private communication) which utilize a [Chabrier \(2003\)](#) initial mass function, [Kriek & Conroy \(2013\)](#) dust law, and solar metallicity. The templates include a range of galaxy types (e.g., star-forming, quiescent, dusty) and realistic star formation histories (SFH; e.g., slowly rising, slowly falling, and bursty).

To validate the photometric redshifts we compared them to 4,513 spectroscopic redshifts in the field from SDSS DR12 (Figure 10), which were mostly at $z < 1$. We found good agreement for objects without complex extended structure (e.g., spiral arms), for which

Table 3. Non-default `eazy-py` configuration parameters used

Parameter	Value
Z_MAX	12
Z_STEP	0.01
SYS_ERROR	0.1
APPLY_PRIOR	False
CAT_HAS_EXTCORR	False
MW_EBV	0
PRIOR_FILTER	134
PRIOR_FILE	‘templates/prior_K_extend.dat’

our photometry extraction was optimized. We found a median offset of $\delta z / (1 + z_{\text{spec}}) = 0.009$, a normalized median absolute standard deviation of $\sigma_{\text{NMAD}} = 0.04$, and a $5\text{-}\sigma_{\text{NMAD}}$ outlier fraction of $< 5\%$. A small population of 41 objects with $z_{\text{spec}} < 1$ were measured to have $z_{\text{phot}} > 4$. These objects were brighter than our brightest candidate $z > 3$ galaxies ($K_s < 18.3$ mag)—none of the 730 fainter objects in the z_{spec} sample were fit at $z_{\text{phot}} > 4$. It is unlikely that objects like these (selected for spectroscopic observations with SDSS) are contaminating our entire high- z galaxy sample. Fainter objects have lower signal-to-noise ratios and therefore have more photometric scatter, so one would expect fainter objects to scatter to higher z_{phot} more often if the population with $z_{\text{spec}} < 1$ and $z_{\text{phot}} > 4$ was due to only random error. On inspection of the photometry of this outlier sample (with $z_{\text{spec}} < 1$ and $z_{\text{phot}} > 4$), we saw complex structure like spiral arms and bars, which were not properly fit by the more simple light-profile models used with our photometry measuring code `Tractor` (See Section 5). Considering that the rest of the sample with $z_{\text{spec}} < 1$ —especially those with fainter fluxes ($K_s > 18.3$ mag) and simpler structures—had measured z_{phot} that were consistent with z_{spec} , we therefore conclude our values z_{phot} are as reliable as can be given the current spectroscopic constraints in this field, though future spectroscopic efforts can better validate this catalog at $z > 1$.

The electronic version of this paper will include a full machine-readable table of our full catalog, including both photometry and EAZY-py properties. A sample of 10 lines of the catalog is given in Table 10 the Appendix, and the full machine-readable table is available with the electronic version of this paper. The photometric redshifts provided in the table are determined by `eazy-py`, using the parameter “`z_phot`” which fits a parabola to the array of χ^2 with respect to redshift across a three

¹¹ Version 0.2.0-16-g6ab4498; <https://github.com/gbrammer/eazy-py>

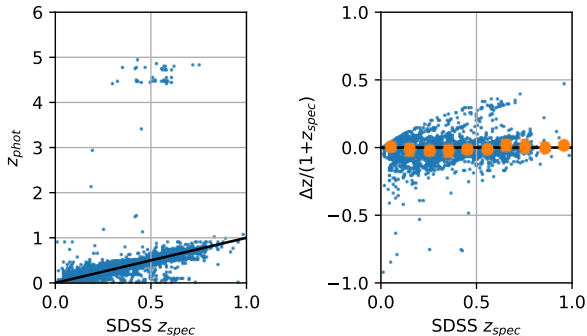


Figure 10. Photometric redshifts compared to spectroscopic redshifts for 4,513 galaxies from SDSS DR12. We find good agreement for objects that have K_s magnitudes in the K_s -magnitude range of our candidate $z = 3 - 5$ galaxy sample ($K_s > 18.3$ mag) implying our sample is free from contamination from objects like those observed in SDSS. The 42 outliers in the upper part of the left panel are due to poor modeling of extended-source structures like spiral arms of bright galaxies, leading to incorrect optical fluxes (see discussion at the end of Section 6).

element window centered on the minimum χ^2 value and finds the minimum of the parabola.

7. MASSIVE QUIESCENT GALAXIES AT $Z = 3 - 5$

While today nearly all massive ($\log M/M_\odot > 11$) galaxies are quiescent, forming few stars, at higher redshifts such galaxies continue to grow. The frontier is now at $z > 3$, where simulations find that nearly all such massive galaxies should be highly star-forming (e.g. Brennan et al. 2015), with massive quiescent galaxies at $z > 4$ being exceedingly rare. Observations find a wide range of quiescent fractions amongst massive galaxies at $z \sim 3$ (e.g. Muzzin et al. 2013; Stefanon et al. 2013), which may be due to small fields covered by most studies. Observations have yet to discover a significant population of massive quiescent galaxies at $z > 4$. As an example of the utility of the NHS K -band selected catalog over $>20 \text{ deg}^2$, here we demonstrate a conservative selection of massive quiescent galaxies at $z > 3$.

7.1. Selection of Massive Galaxies at $3 < z < 5$

We selected $z = 3 - 5$ galaxies using criteria based on photometric cuts and properties of the photometric redshift (z_{phot}) probability distribution functions (z PDFs) similar to the procedure outlined by Finkelstein et al. (2015a). Prior to these EAZY-based cuts, we required a $5\text{-}\sigma$ or greater detection significance in K_s , a $2\text{-}\sigma$ or greater detection significance in IRAC $3.6 \mu\text{m}$, and a u' -band $S/N < 2$, as the Lyman break falls red-ward of the u' band in galaxies at $z > 3$. We also required a measurement (but not necessarily a detection) in all 5

optical DECam bands to ensure reliable constraints on z_{phot} .

One limitation of our study is that red galaxies at low redshift can have SED shapes that appear similar to our $z = 3 - 5$ galaxies within our filter set. We discussed this topic in the context of existing SDSS spectral observations in our field in Section 6. The degeneracy of these objects in optical and IR photometry was investigated by Dunlop et al. (2007) and motivated the inclusion of a red, dusty template in eazy-py (Brammer et al. 2008) to account for the presence of these objects. This results in several potential candidate high-redshift quiescent galaxies having small peaks in their $P(z)$ distributions at $z < 2$. Because the abundance of red galaxies at $z < 2$ is likely much higher than at $z > 2$, this could potentially lead to high contamination rates.

One way to mitigate this is to use an apparent magnitude prior, which applies a Bayesian prior based on a source’s apparent magnitude. EAZY has a built in such a prior, devised based on the luminosity functions from the De Lucia & Blaizot (2007) semi-analytic model (see Brammer et al. 2008 for details). These priors are typically peaked at low-redshift with a tail to higher redshift, with the tail becoming more prominent at fainter magnitudes. As our goal here is simply to demonstrate the utility of the NHS catalog for discovering massive quiescent galaxies at $z > 3$, we elect to make use of this prior when calculating photometric redshifts for this analysis to minimize contamination as much as possible. For bright sources, the application of this prior will typically result in any low-redshift solutions becoming the dominant one, even if the higher-redshift solution was a better fit to the photometry. We note that this likely results in significant incompleteness in our sample. The simulation used for this prior used only a 1 deg^2 light cone, thus does not have the volume to constrain the abundance of the rare sources we seek here. Additionally, as this simulation is >10 years old, it would not have made use of the advances in galaxy feedback physics made over the intervening years which have increased the efficiency of quenching in more modern simulations. Nevertheless, here we include the prior to ensure a conservative selection, and we will revisit the prior in a future work.

We applied the following four selection requirements based on the EAZY z_{phot} and stellar mass results, using the results ran with the apparent magnitude prior:

1. the highest peak of the z PDF must fall at $z > 3$,
2. the integral of the normalized z PDF between $3 \leq z < 5$ must be greater than or equal to 0.6, which ensures a majority of the z PDF integrated probability is in the redshift range of interest,

Table 4. Candidate Massive Quiescent Galaxies

ID	RA	Dec	K_{AB}	z_p	$\int P(z_p) > 3$	$\log(M_*)$	$\log(\text{sSFR})$	$\log(M_*)$	$\log \text{sSFR}$	$\int P(\text{sSFR}) < -10.05$
	(J2000)	(J2000)				EAZY	EAZY	BC03	BC03	BC03
	(deg)	(deg)	(mag)			(M_\odot)	(yr^{-1})	(M_\odot)	(yr^{-1})	
67411	14.996527	-0.347113	19.9	3.87	0.71	12.3	-11.4	12.3	-11.0	0.95
291064	16.754635	-0.028062	20.7	4.63	0.90	12.2	-10.2	12.2	<-11.5	0.98
311951	16.762005	-0.358180	20.6	4.63	0.95	12.4	-10.1	12.4	-10.3	0.74
344891	17.027281	-0.697423	20.4	3.43	0.84	11.9	-11.5	11.9	<-11.2	0.97
386425	17.379851	0.729148	20.3	3.99	0.76	11.7	-11.1	11.7	<-11.0	0.96
664819	19.731433	0.492264	21.0	4.65	0.89	11.7	-10.2	11.7	<-11.0	0.77
1055967	22.746300	0.370704	20.6	4.03	0.87	12.2	-11.6	12.0	-10.3	0.92
1198361	24.057372	0.135012	20.8	4.44	0.99	11.9	-10.3	11.8	-10.6	0.71
1208324	23.806994	-0.483853	19.6	4.15	1.00	12.0	-10.1	12.0	<-11.3	0.99

NOTE—Properties of the final sample of nine candidate massive quiescent galaxies. ^aObjects with $\text{SFR}_{BC03} < 5 M_\odot \text{ yr}^{-1}$ have their sSFR listed as an upper limit derived with this limiting value (corresponding roughly to the UV-based SFR at the limit of the DECam optical imaging).

- the best-fitting template from `eazy-py` must have a $\chi^2 < 10$
- the best-fitting stellar mass $> 10^{11} M_\odot$

This sample of massive ($\log M/M_\odot > 11$) high-redshift ($3 < z < 5$) consists of 466 galaxy candidates from our full catalog. We reiterate that this is a lower limit on the true number, due to the use of the luminosity prior which increases the fidelity of our sample at the cost of increased completeness.

7.2. Selecting Massive Quiescent Galaxies

It is common to separate quiescent galaxies from star-forming galaxies using a selection box in the rest-frame $U-V$ vs $V-J$ diagram (UVJ diagram; e.g., [Labbé et al. 2005](#); [Wuyts et al. 2007](#); [Whitaker et al. 2011](#); [Muzzin et al. 2013](#)) given the bi-modality of galaxies in color and SFR (e.g., [Kauffmann et al. 2003](#)) even at high-redshift (e.g., [Bell et al. 2004](#); [Brammer et al. 2009](#)). Another separation method used is setting a threshold in sSFR derived from SED-fitting, which has been found to correlate with UVJ diagram classifications up to $z = 2.5$ (e.g., [Williams et al. 2010](#)).

We select candidate quiescent galaxies from this parent massive galaxy sample using sSFR. To decide on the appropriate sSFR threshold, one must consider the evolution in the galaxy main sequence, where galaxies at fixed stellar mass have higher average star-formation rates at higher redshift (e.g., [Noeske et al. 2007](#); [Whitaker et al. 2014](#); [Salmon et al. 2015](#)). We use the relation found by [Salmon et al. \(2015\)](#) at $z = 4$

to decide on a sSFR cut. They find $\log(\text{SFR}/M_\odot/\text{yr}) = 0.7 \log(M/M_\odot) - 5.7$ using a sample of galaxies spanning $8.5 < \log(M/M_\odot) < 10.5$, with a 1σ scatter of 0.35 dex in SFR at fixed stellar mass. Extrapolating mildly to our stellar mass threshold of $\log(M/M_\odot) = 11$, this relation predicts the typical galaxy should have $\log(\text{SFR}/M_\odot/\text{yr}) = 100 M_\odot \text{ yr}^{-1}$, for a $\log(\text{sSFR}/\text{yr}^{-1}) = -9$. To classify a galaxy as quiescent, we require it to have a SFR which is 3σ below this threshold. This corresponds to a $\text{SFR} = 8.9 M_\odot \text{ yr}^{-1}$, or $\log(\text{sSFR}/\text{yr}^{-1}) < -10.05$. Applying this sSFR cut to the initial massive galaxy sample results in a sample of 51 candidate massive quiescent galaxies.

While we chose to use `EAZY-py` to fit the stellar population properties and photometric redshifts for its speed (as we ran this on our full catalog), `EAZY-py` does not calculate uncertainties on the physical properties. This is not desirable, as some properties, particularly sSFR, may have wide posteriors. We thus ran a second iteration of SED fitting on these 51 candidate massive quiescent galaxies, both to vet the results from `EAZY-py`, and also to generate parameter posterior distributions. For this second method, we used the grid-based Monte Carlo SED fitting method developed by [Finkelstein et al. \(2015b\)](#), utilizing the stellar population models of [Bruzual & Charlot \(2003\)](#). This method finds the best-fit via a maximal likelihood search of the parameter space, deriving posterior distributions on those parameters via a Monte Carlo analysis. The addition of this analysis allows us to test how well our derived stellar population properties agree when using both dif-

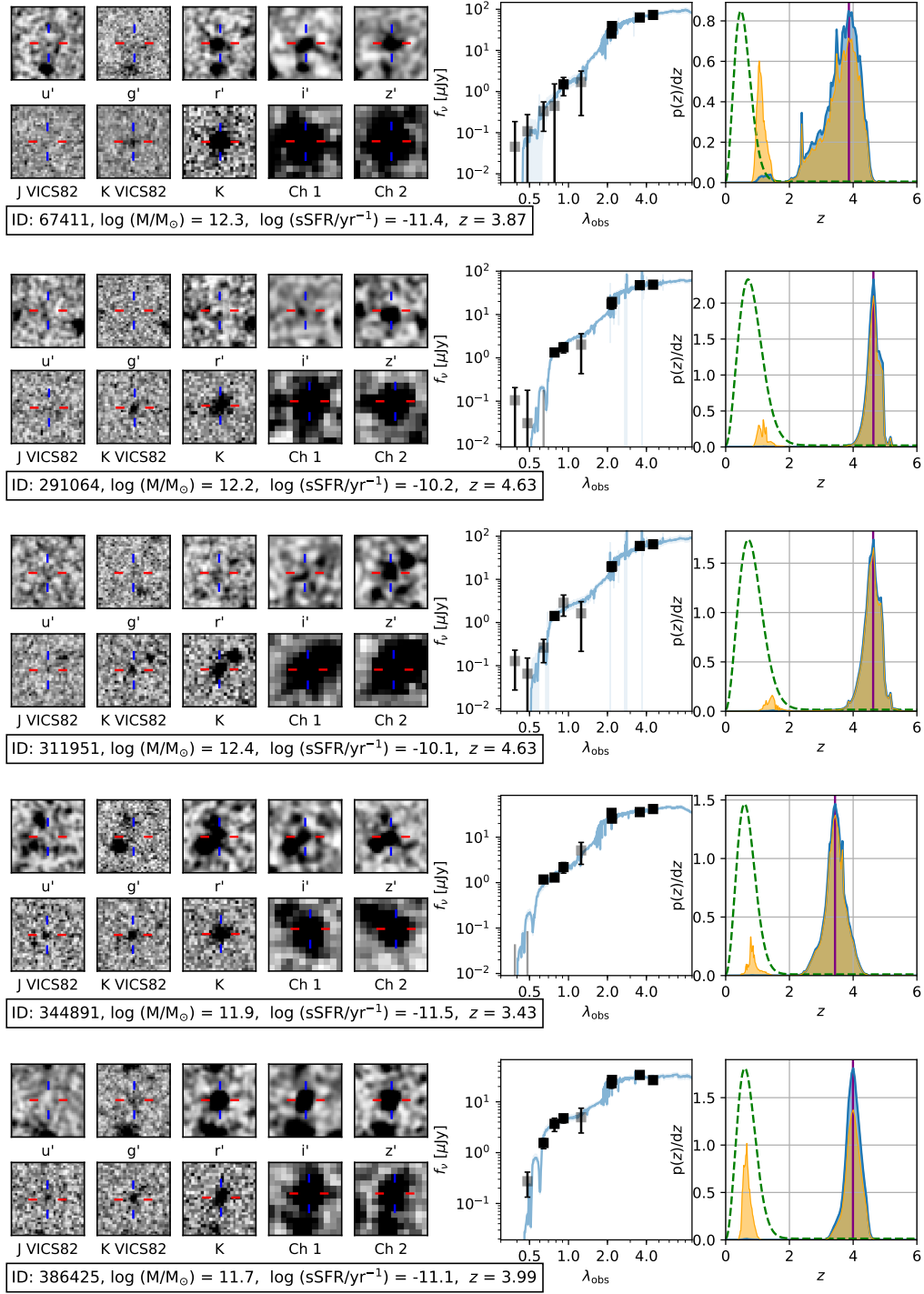


Figure 11. For the first five of nine of our massive, quiescent, $z = 3-5$ galaxy candidates: photometric images (left), best-fitting templates with the photometry (center), and z PDF (right). The images are $10'' \times 10''$ in all bands. The squares in the middle plot show the observed photometry, shown in gray when the S/N is less than 2. The blue-shaded curve shows the measured $P(z)$ before convolving with the prior (shown in green), while orange shows the result after convolution, with the vertical line denoting the best-fitting redshift after convolution.

ferent stellar population models, and a different fitting method.

The agreement in stellar mass between these two methods is very good, with all 51 candidates having $\log(M/M_\odot) > 11$, with the mass difference < 0.3 dex for

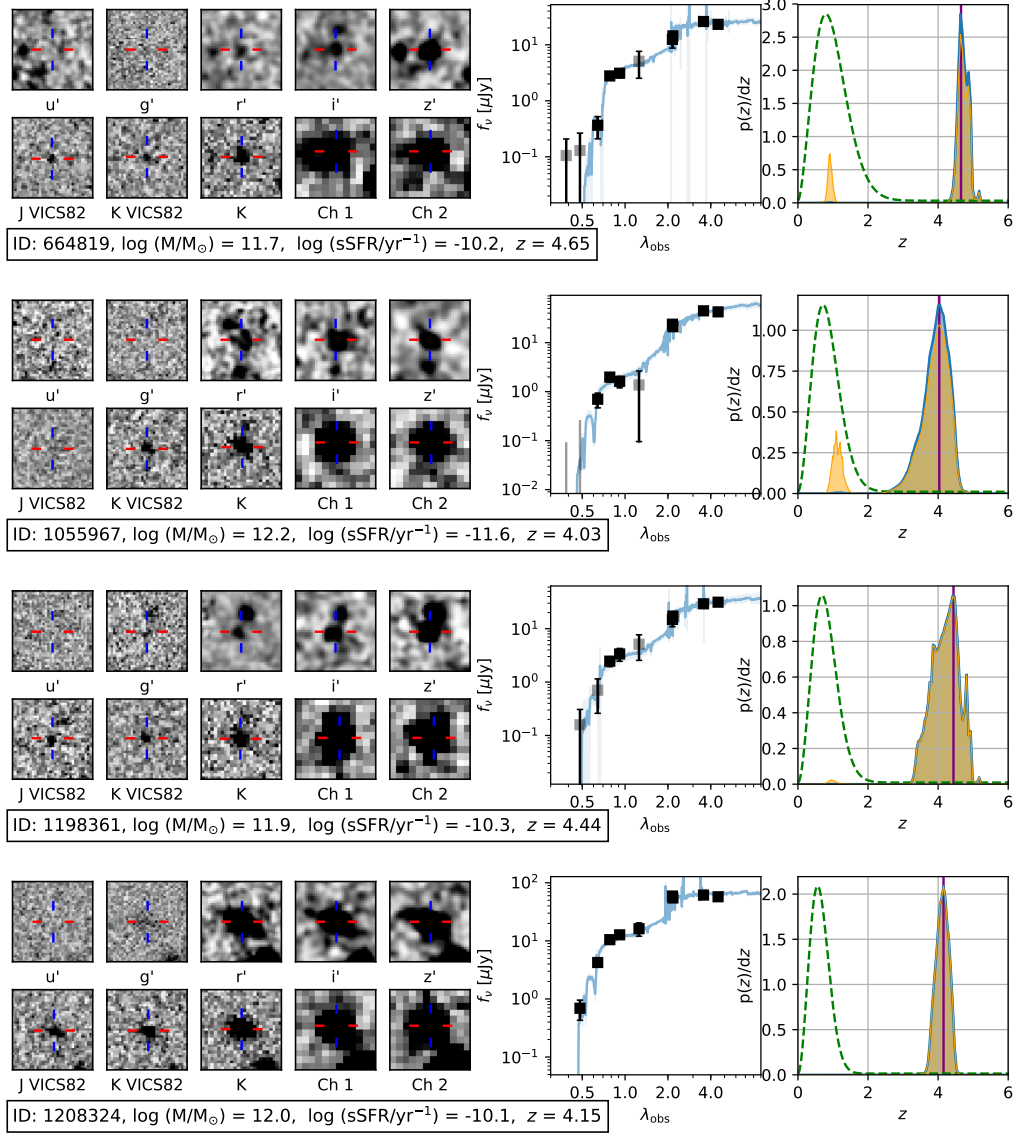


Figure 12. Same as Figure 11, for the final four candidates.

90% of the sample, with a maximum difference of 0.6 dex. The difference in SFR is however larger, with EAZY-py resulting in systematically higher SFRs by ~ 0.5 dex, and only $\sim 30\%$ of the sample having SFR differences of < 0.5 dex. Due to the potential for large differences in the inferred SFR from the use of different modeling codes and templates, we further hone our candidate list by requiring galaxies to have $\log(M/M_{\odot}) > 11$ and $\log(\text{sSFR}/\text{yr}^{-1}) < -10.05$ from both methods. This reduces the sample from 50 to 23 candidates. For this reduced sample, the SFRs agree very well with a median difference of zero, and a standard deviation of 0.6 dex.

To further examine the validity of these candidates, we make use of the posterior distributions made available

by the additional BC03-based SED fitting to explore how confident we can be that these sources are quiescent. We calculated the integral of the sSFR posteriors which were below our sSFR cut. We found that most sources had relatively high values, indicating tight sSFR posteriors centered at low values, but there were a few with very wide sSFR posteriors leading to small values of this integral. We thus apply one final cut to our sample, requiring that $> 68\%$ of the sSFR posterior satisfy our sSFR cut (< -10.05). This removes five additional sources, leaving 18 candidate quiescent galaxies.

As a final quality check on our candidate galaxies, we visually inspected these 18 candidates. We found that five candidates had potential problems with their photometry - four had visible smudges in the u -band,

which while not formally exceeding 2σ , visually appeared above the noise and coincident with the source position, while one source had no VISTA measurements due to bad pixels in both J and K at the source position, leaving the 4000\AA break poorly constrained. Four more sources appear visibly elongated, and have half-light radii (r_h) measurements $\gtrsim 1''$, and are thus significantly resolved (bright, unresolved sources in this catalog have $r_h = 0.7 \pm 0.1''$). This corresponds to a physical half-light radius of ~ 7 kpc at these redshifts, highly unlikely for massive galaxies at $z \sim 4$ as trends at lower redshifts would predict $r_h < 1$ kpc (e.g., van der Wel et al. 2014). While these nine sources formally satisfy our selection criteria, this visual inspection casts doubt on their validity, thus we remove them from our high-confidence sample. All nine of these removed candidates are shown in the Appendix in Figures 15 and 16, and are listed in Table 9.

We show our final sample of nine candidate massive quiescent galaxies in Figures 11 and 12, with relevant quantities for these galaxies listed in Table 4.

7.2.1. Comparison to UVJ Selection

In Figure 13, we show our $z = 3 - 5$ massive quiescent galaxy candidates in two $U - V$ vs $V - J$ diagrams to inspect where they fall with respect to a relevant UVJ selection box. We show both the nine higher-confidence sources, the nine sources we removed to the appendix, and the full parent sample of 466 massive galaxies. The color of the symbols denote the $\log \text{sSFR}/\text{yr}^{-1}$. In each panel we include the selection box from Muzzin et al. (2013) for reference. The quiescent galaxies form a locus that is offset from the diagonal part of the reference selection box (bluer in both colors by up to 0.5 mag) with the majority of our sSFR-selected quiescent galaxies falling outside of the UVJ selection box. We also see that a fraction of objects with $\log \text{sSFR}/\text{yr}^{-1} > -11$ fall into the UVJ selection box, so had we used this UVJ selection box to select quiescent galaxies our SED modeling implies that we would have been very incomplete to quiescent galaxies and selected a number of star-forming galaxies.

This issue with the UVJ diagram has been seen before. A study of passive galaxies at $z > 3$ in the GOODS-South field by Merlin et al. (2018), who selected passive galaxies using SED fitting, found an offset between their sSFR-selected passive galaxy candidates and the nominal UVJ diagram selection box. They note that a UVJ selection of passive galaxies is incomplete, and that if a top-hat SFH (where galaxies form stars continuously for some time, and then quench) is assumed, galaxies are quiescent for ~ 0.5 Gyr before they enter the

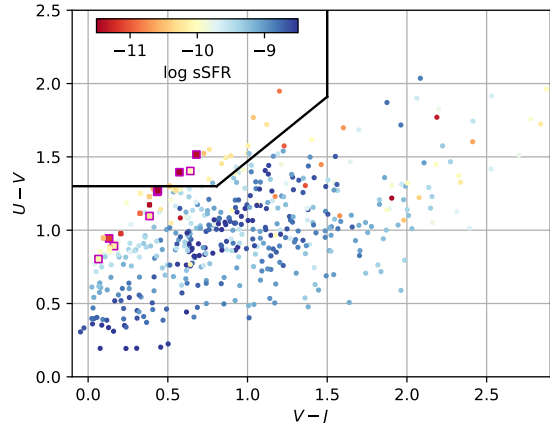


Figure 13. UVJ diagram for massive ($\log M/M_\odot > 11$) at $3 \leq z < 5$. The symbol color encodes the sSFR from EAZY-py. Squares denote our massive quiescent candidates (with those outlined in larger magenta boxes coming from the final higher-confidence sample of nine sources), while circles denote star-forming galaxies. A substantial portion of the quiescent galaxies selected via a sSFR threshold fall outside of the selection box from Muzzin et al. (2013), suggesting a custom selection box would be required for our sample. However, such a selection box would also include a significant number of star-forming galaxies, highlighting the utility of our sSFR-based selection.

UVJ selection box from below, similar to the locus of our candidate sample. This can be seen in Fig 13, where the candidates with the lowest sSFR fall in the selection box, but those closer to our $\log \text{sSFR}/\text{yr}^{-1} > -11$ threshold (which likely have had less time since quenching than the lowest sSFR objects) fall outside of it. Since galaxies at $z > 4$ exist when the Universe is < 2 Gyr old, it is not surprising that these quiescent galaxies may not have been quenched for > 0.5 Gyr. In this sense, our galaxies may be more analogous to post-starburst galaxies local rather than fully quenched galaxies. Similar conclusions have been reached by other studies in this epoch (e.g., Marsan et al. 2020; D’Eugenio et al. 2020; Forrest et al. 2020b).

7.3. Properties of Candidate Massive Quiescent Galaxies

As listed in Table 4, and shown in the right panel of each candidate’s plot, the $P(z)$ distributions for our nine candidates strongly prefer high-redshift. Though we required $\int P(z > 3) > 0.6$, 7/9 candidates have this quantity > 0.8 . This is understandable due to our use of the prior, shown as the green line in the $P(z)$ panel for each object. Objects which have even small $P(z)$ secondary peaks where this prior is significantly non-zero will have $P(z)$ which strongly prefers a low-redshift

solution after folding in the prior, hence these objects do not satisfy the sample-selection criteria.

To enable both robust photometric selection, and decent constraints that a galaxy is quiescent, we would expect the SED to show a Lyman break (e.g., no significant flux in the u -band, and a decrement in the g -band), weak non-ionizing UV flux, and a significant Balmer break, with a roughly flat SED redward of $2 \mu\text{m}$. Inspecting the candidates, this description is broadly characteristic of our sample. The best-fit model follows the photometry closely, which is expected given our stringent χ^2 cut.

By definition, our sample should have large stellar masses, and given our criteria selecting for highly robust quiescent solutions over a very large volume, we should expect to be discovering amongst the most massive galaxies in this epoch. However, it is surprising that we find several (5/9) galaxies with $\log M/M_\odot > 12$. Upon investigation of the stamp images, several of the sources do show nearby neighbors, which could be affecting the photometry and subsequent stellar mass values. We found that every neighbor was present in the input catalog, either due to being detected in the NHS K_s catalog, or in the DECam (for very blue sources) or IRAC (for very red sources). This ensures that TPHOT is modeling each source separately. We are confident that the ground-based fluxes are accurate, as these neighbors appear well resolved. This is less certain in IRAC due to the larger PSF. While TPHOT is designed for these situations, it is possible that the IRAC measurements of our sources contain some residual flux from these neighbors, biasing the stellar masses high. Even if the deblending is accurate, it is possible that these neighbors are gravitationally lensing our candidates by a factor of \sim a few (e.g. Mason et al. 2015) due to their close proximity. Finally, galaxies this massive may have some of their light contributed due to AGN activity. Though this is unlikely to dominate the luminosity due to the stellar appearance of the SED, it could also contribute primarily to the IRAC fluxes, biasing the masses high.

Although we have discussed a few reasons why these extremely massive galaxies may have true stellar masses lower by a factor of \sim a few, it is worth exploring how surprising their presence is. Ideally we would compare to published stellar mass functions from observations or simulations, but as we are the first to explore galaxies in this epoch over such a large volume, such an idea comparison does not exist. Perhaps the easiest comparison is to Sherman et al. (2020a), who used this same NHS catalog to select galaxies up to $z \sim 3$. Over our same area, they found 198 and 12 galaxies at $\log(M/M_\odot) > 11.5$ and 12.0, respectively, at $z = 3.25$. Muzzin et al. (2013)

calculated the stellar mass function at $z = 3.5$ over 1.6 deg^2 , with these functions predicting 692 and 22 galaxies at $\log(M/M_\odot) > 11.5$ and 12.0, respectively, over our area of 17.5 deg^2 . Finally, Davidzon et al. (2017) calculated the stellar mass function at $z = 4$ over 2 deg^2 , which would predict 59 and 0 galaxies at $\log(M/M_\odot) > 11.5$ and 12.0, respectively, over our area.

Collectively, these previous results show that the presence of $z > 3$ galaxies at $\log(M/M_\odot) > 12.0$ is not unprecedented, but the large dispersion in these results suggests that their abundance is not well quantified. We also note that these predicted numbers rely on the extrapolation of a Schechter function, which assumes an exponential cutoff, while the shape of the massive end of the stellar mass function hasn't been observationally validated at these redshifts. On the theory side, Behroozi & Silk (2018) found that in a SHELA-like survey at $z = 4$ the presence of several galaxies with $\log(M/M_\odot) > 12$ does not violate constraints on the growth of structure from ΛCDM (extrapolating their Figure 2 to $z = 4$; P. Behroozi, private communication). Additionally, the SIMBA numerical hydrodynamics simulation (Davé et al. 2019) contained 3 galaxies with $\log(M/M_\odot) > 12$ at $z = 3$ over a relatively small volume (143^3 cMpc^3). None of these massive were present at $z = 4$, though the simulation did contain five $z = 4$ galaxies with $\log(M/M_\odot) > 11.5$.

While observations and theory thus don't prohibit the presence of these massive galaxies, clearly further observations are needed to better prove the validity of these sources. First and foremost, confirmation via spectroscopy that these sources are at the estimated redshifts would remove the strongest concern, that the sample is contaminated by lower-redshift sources. As these galaxies still have some low-level residual star formation, this may be possible via [O II] emission with ground-based K -band spectroscopy. Lacking emission lines, confirmation via stellar absorption lines is possible, though this will likely require the sensitivity of the *James Webb Space Telescope* (*JWST*). Further improvement on the SED constraints are also possible, as better removal of low-redshift solutions (needed to keep true candidates from being removed with application of the magnitude prior) can be obtained with deeper u and g -band imaging. Likewise, better constraints on the star-forming properties can be obtained with deeper near-infrared imaging with, for example, FLAMINGOS-2 or NIRI on Gemini in the near-term, or *JWST* in the longer-term. Finally, dust-continuum observations with ALMA can rule out both low-redshift dusty contaminants, as well as significant obscured star-formation in $z \sim 4$ galaxies. The combination of the large volume probed by our catalog

with these followup observations will ultimately allow large samples of confirmed massive quiescent galaxies to be formed, challenging theoretical models of galaxy formation.

7.4. Comparison with Previous Results

At $z \sim 2-3$, using this same NEWFIRM catalog [Sherman et al. \(2020b\)](#) and [Florez et al. \(2020\)](#) explored the quiescent fraction amongst massive galaxies, and found it to be $\sim 20-25\%$ using a similar selection as we employed. Moving to $z > 3$, [Muzzin et al. \(2013\)](#) performed the previous widest-area search for quiescent galaxies (1.6 deg^2), using a UVJ selection to find 28 massive quiescent galaxies and 146 star-forming galaxies with $\log M/M_\odot > 10.94$ at $3 \leq z < 4$. [Stefanon et al. \(2013\)](#) found four candidate massive compact quiescent galaxies at $z > 3$, though their stellar mass threshold was lower due to their smaller volume (the search encompassed the CANDELS fields). [Spitler et al. \(2014\)](#) used UVJ selection to find that roughly *half* of a sample of $\log (M/M_\odot) > 10.6$ galaxies were quiescent using the zFourGE survey over a subset of the CANDELS fields (see also [Straatman et al. 2014](#)).

Studies have also recently been successful spectroscopically confirming these massive quiescent galaxies at $z \sim 3-4$ and ruling out significant levels of obscured star-formation with ALMA (e.g. [Glazebrook et al. 2017](#); [Valentino et al. 2020](#); [Santini et al. 2019](#); [Marsan et al. 2020](#); [Schreiber et al. 2018](#); [Tanaka et al. 2019](#); [D’Eugenio et al. 2020](#); [Forrest et al. 2020a,b](#)). Though these surveys have different selection techniques, mass limits, and volumes, together they collectively show that massive quiescent galaxies exist in some non-zero abundance at $z > 3$.

We compare our measurements directly to predictions from two recent simulations. The first is the updated “Santa Cruz” semi-analytic model (SC-SAM [Somerville et al. 2015](#); [Somerville et al. 2008](#), Somerville et al., in prep). The SC-SAM includes standard recipes for the main processes in galaxy formation, such as gas cooling, star formation, and stellar feedback, and implements AGN feedback in two modes: thermal energy deposition from a low-accretion rate, radiatively inefficient “jet mode” (which can offset cooling flows), and ejection of cold interstellar gas via radiation pressure from rapidly accreting, radiatively efficient black holes (see [Somerville et al. 2008](#), for more details). To calculate the quiescent fraction from this model, we made use of the lightcones created for the CANDELS project, which consist of eight realizations of each of the five CANDELS fields, for 40 realizations total. The combination of these lightcones results in a total area of 11.9 square

degrees, corresponding to a substantial volume of 0.28 Gpc^3 at $3 < z < 5$, or roughly 70% of what we probe observationally¹². This yields 576 SAM galaxies in our redshift and mass range of interest. As all of the SAM galaxies have $\log M/M_\odot < 11.4$, we can only compare over a narrow mass range. Of the 576 SAM galaxies, only 25 meet our definition of quiescence, for a quiescent fraction of 4.3% from this simulation. However, all of these quiescent sources have $z < 4$, thus this model is in tension with our observations in that it both produces no quiescent galaxies at $z > 4$.

We also compare to recent results from the SIMBA numerical hydrodynamics simulation ([Davé et al. 2019](#)). SIMBA is the successor to the MUFASA simulations, and is run with the GIZMO meshless finite mass hydrodynamics scheme. SIMBA included updated sub-grid prescriptions for star formation and stellar driven outflows, and one of the most sophisticated and physically motivated treatments of black hole growth and AGN feedback in any available cosmological simulation. Like the SC-SAM, SIMBA implements two modes of AGN feedback, which are differentiated based on the accretion rate of the black hole. An important caveat is that the volume of this simulation is rather limited, $\sim (143 \text{ Mpc})^3 \sim 3 \times 10^6 \text{ Mpc}^3$, which is $\sim 1\%$ of our survey volume. At $z = 3$, SIMBA has 109 massive galaxies with $\log M/M_\odot > 11$. However, only 10 of these galaxies have $\text{sSFR} < 10^{-10} \text{ yr}^{-1}$. At $z = 4$, there are 30 massive galaxies, though none meet our definition of quiescence, while there are still a significant number of observational counterparts. We discuss possible interpretations of the discrepancy between both theoretical predictions and the observational results in Section 8.

8. DISCUSSION

Our discovery of a potential population of massive quiescent galaxies at $z = 3 - 5$ has significant implications for understanding the physical processes that shape the formation and evolution of galaxies. If followup observations confirm the existence of massive quiescent galaxies at $z \sim 4-5$, when the universe was only 1.2-1.5 Gyr old, implies that the universe can rapidly build galaxies 1-10 times the mass of the Milky Way and quench their star formation in a very short time. If the first galaxies start to form around 0.3-0.4 Gyr after the Big Bang, this leaves less than 1 billion years for massive quiescent galaxies at $z \sim 5$ to grow. It is unclear whether the same

¹² However, it should be kept in mind that these lightcones were drawn from an N-body simulation with a total volume of $4.56 \times 10^7 \text{ Mpc}^3$, and unlike in the real Universe, the structures along the line of sight are not independent.

mechanisms that are responsible for forming quiescent galaxies at $z = 0 - 2$ can be responsible for forming their counterparts at $z > 5$.

Several previous studies have examined theoretical predictions for quiescent fractions at $z = 0 - 2$ and identified a number of mechanisms or formation paths that may be responsible. [Kimm et al. \(2009\)](#) analyzed several different semi-analytic models and quantified the fraction of quiescent galaxies as a function of internal properties and environment, compared with group catalogs extracted from the Sloan Digital Sky Survey.

[Brennan et al. \(2015\)](#) compared observations of the evolution of the massive quiescent galaxy fraction (using their own analysis of the CANDELS fields, finding a quiescent fraction of $\sim 30\%$ at $z = 3$) to a previous generation of the Santa Cruz semi-analytic model, where passive spheroids are built up via AGN feedback originating from major and minor mergers and disk instabilities. In both observations and simulations, rather than a constant threshold in sSFR, they imposed a cutoff based on the offset in SFR from the star-forming main sequence at a given redshift. Their simulations predict a quiescent fraction which is in reasonable agreement with $z \sim 0$ observations, but drops to zero by $z \sim 2.5$, becoming increasingly discrepant with observations at increasing redshifts.

In the hydrodynamical cosmological simulation Illustris, [Wellons et al. \(2015\)](#) investigated the formation of compact massive galaxies in a box of 106.5 co-moving Mpc on a side. They found two main formation paths for compact massive galaxies at $z = 2$: (1) early formation when the universe was denser, and (2) a central burst of star formation from a major merger. The first path consisted of formation early in the universe ($\log M/M_\odot \sim 10$ before $z \sim 7$) and smooth stellar mass growth at a rate less than the typical galaxy of similar mass until $z \sim 4$ when the stellar mass exceeded $\log M/M_\odot = 11$. At that time, the feedback from the SMBH began to significantly decrease the SFR, quenching the galaxy by about $z \sim 2.5$. In the simulation, this path produced a massive galaxy at $z \sim 4$, however, the galaxy was not quenched ($\log \text{sSFR} < -11 \text{ yr}^{-1}$) until $z \sim 2.5$ after 1 Gyr of SMBH feedback. The second path involved an intermediate mass galaxy growing at a typical SFR for its mass, from early times to $z \sim 2.5$ when a wet major merger caused the SFR to spike and the stellar mass to double to $\log M/M_\odot > 11$. The wet major merger also caused accretion onto and feedback from the central SMBH decreasing the SFR. However, once again the decrease is gradual; if we were to apply these scenarios to our observational sample, we would indeed be able to create massive galaxies by the $z \sim 5$ epoch, but the ob-

jects would not be classified as quiescent until well after our redshift window.

The successor of the Illustris simulations, IllustrisTNG, included an updated kinetic implementation of "jet mode" AGN feedback ([Weinberger et al. 2017, 2018](#)), in part to correct the weak color distribution bimodality between red and blue galaxies found in the original Illustris simulations ([Nelson et al. 2018](#)). [Taccella et al. \(2019\)](#) explores the build-up of spheroids and discs in IllustrisTNG and finds the most massive ($\log M/M_\odot = 11.5$) galaxies at $z = 0$ grow more slowly in situ, not reaching $\log M/M_\odot > 11$ until $z \sim 1$. In these galaxies, SMBH feedback becomes effective at ceasing star formation when the SMBH mass exceeds $\log (M_{BH}/M_\odot) \sim 8.2$ around $z \sim 2$, when the growth of stellar mass becomes dominated by mergers. The faster and more efficient SMBH feedback in IllustrisTNG can quench massive galaxies quickly, however, the implementation of strong feedback at all times appears to slow the in situ growth of galaxies and prevent massive systems from forming at early times. Figure 7 of [Merlin et al. \(2019\)](#) shows the number density of quiescent galaxies with stellar mass greater than $5 \times 10^9 M_\odot$ extracted from the original Illustris simulations and from the IllustrisTNG 100 and 300 boxes, defining quiescence as $\text{sSFR} < 10^{-11} \text{ yr}^{-1}$. With the major caveat that the stellar mass limit of the sample they have extracted from simulations is *much* lower than the one we have been considering, they show that IllustrisTNG has a significantly larger number density of quiescent galaxies at $3 \lesssim z \lesssim 4$ than the original Illustris or SIMBA simulations, but the number of quiescent galaxies drops steeply at $z > 3.5$. Their comparison shows that the EAGLE simulations ([Schaye et al. 2014](#)) predict the highest number density of quiescent galaxies at $z \gtrsim 3.5$ of any of the simulations they considered.

Non-black-hole-related mechanisms have also been proposed for quenching massive galaxies, including morphological quenching and environmental quenching. Morphological quenching is the suppression of star-formation in a gaseous disk inside a spheroidal galaxy due, in part, to the tidal forces of the stars preventing fragmentation in the gaseous disk. [Martig et al. \(2009\)](#) demonstrated this mechanism with a massive galaxy growing relatively slowly at low redshift, from $\log M/M_\odot = 10.5$ at $z = 2$ to $\log M/M_\odot = 11$ by $z \sim 0.8$, spanning ~ 4 Gyr. For morphological quenching to work in the early universe, it would have to work on much shorter time scales than has been demonstrated, though high-resolution imaging of our sample could at least determine if they even have spheroidal morphologies. Environmental quenching via ram pressure or

tidal stripping of gas can operate on satellite galaxies in dense environments, but the majority of galaxies in our sample are unlikely to fit these criteria.

There is now a general consensus that physical processes related to the radiation and kinetic energy emitted by accreting SMBHs (AGN feedback) are the dominant mechanism for quenching star formation in massive galaxies. For example, (e.g. [Su et al. 2019](#)) showed that previously proposed processes such as gravitational heating and morphological quenching are not viable on their own — only SMBH-related processes can lead to long-lived quenching – reducing the SFR well below the star-formation main sequence and keeping it there.

Most current semi-analytic models, as well as most numerical cosmological hydrodynamic simulations (e.g., IllustrisTNG, HorizonAGN, Romulus) make assumptions that cause feedback from radiatively efficient accretion onto a SMBH to be inefficient at quenching, or to quench only over a short timescale. Feedback from a low-accretion rate, radiatively inefficient “jet mode” is responsible for strong, sustained quenching in massive central galaxies in both the Santa Cruz SAM and in IllustrisTNG. However, more detailed modeling of “radiative” feedback from more rapidly accreting black holes has shown that this process may drive powerful, high velocity winds (as observed ubiquitously in AGN hosts) which can not only remove the cold dense gas from the interstellar medium of galaxies, leading to strong rapid quenching, but also prevent further accretion of gas over timescales of many Gyr ([Choi et al. 2015, 2017](#); [Brennan et al. 2018](#); [Pandya et al. 2017](#)). To date these simulations have only been carried out as “zoom-ins” of a few tens of massive halos, so it is not possible to compute a statistical quenched fraction. However, it is clear that this feedback mode will be effective at higher redshifts than the “jet mode,” which requires more massive black holes, lower accretion rates, and the development of a hot circumgalactic halo (“working surface”), all of which develop only at later cosmic epochs. Some hydrodynamic simulations, such as EAGLE and SIMBA, have included an implementation of the “strong radiative mode” quenching in cosmological volumes. SIMBA produces a population of “fast-quenched” galaxies which are more prevalent at early epochs ([Rodríguez Montero et al. 2019](#)), but the early quenching is typically not sufficient to drop below $\text{sSFR}=10^{-10} \text{ yr}^{-1}$ at $z > 4$, even though it drops the sSFR by an order of magnitude relative to the main sequence. Currently these simulation volumes tend to be fairly small, (~ 100 Mpc on a side), so it is not yet possible to robustly study the statistical properties of such massive galaxies as the ones in this study.

It is important to note when comparing results that different observational and theoretical studies often employ different definitions of quiescence. Most deal with the degree of quiescence, either as we do by imposing a single sSFR threshold, or as [Brennan et al. \(2015\)](#) have done by looking at how reduced the SFR is compared to the main sequence, which takes into account the redshift dependence of the SF main sequence normalization. Another important question is the timescale of this quiescence – how long did it take for the galaxies to become quiescent — is the process of quenching slow or fast? Are the galaxies permanently quenched, or will they become star-forming again in the future? The former can be addressed empirically by constraining the star-formation histories of our quenched galaxies to explore how long they have been quenched, which we will address in future work. Constraints on quenching timescales can provide even more powerful tests of the physical processes responsible for quenching in theoretical models ([Pandya et al. 2017](#)).

9. SUMMARY

In this paper, we have presented the K_s -selected catalog of the NEWFIRM HETDEX Survey (NHS) within the SHELA field. The catalog has a moderate depth ($K_s \sim 22.4$ mag, 5σ) and is unique in covering a wide $\sim 22 \text{ deg}^2$ area. When combined with the existing extensive multi-wavelength dataset in the SHELA field, the volume probed by the NHS data allows for the detection of the most statistically significant population of massive galaxies at high redshift assembled to date.

We derive photometric redshifts, stellar masses and rest-frame colors for massive ($\log M/M_\odot > 11$), star-forming and quiescent galaxies between $z = 3 - 5$ using the SED-fitting code `eazy-py`. We select galaxies using a procedure utilizing the zPDF and define quiescence with a sSFR threshold ($\log \text{sSFR}/\text{yr}^{-1} < -10.05$; 3σ below the $z = 4$ main sequence of [Salmon et al. 2015](#)). We utilize an extremely conservative (allowing for potential incompleteness) selection process to identify a sample of nine massive quiescent candidates out to $z \sim 4.7$. We locate our sSFR-threshold-based quiescent galaxy sample on the UVJ diagram and find our sample occupies a parameter space not typically selected by past studies utilizing the UVJ selection method, suggesting these candidate galaxies are post-starburst in nature, and not yet fully quenched. These results imply that there exists a population of massive galaxies at even higher redshifts that have rapidly formed their stars and have been quenched in less than ~ 1.5 Gyr since the Big Bang.

We compare our results with the predictions of two different theoretical cosmological simulations of galaxy

formation, which incorporate physical prescriptions for feedback from accreting SMBHs: the Santa Cruz semi-analytic model and the SIMBA hydrodynamic simulation. Both simulations reproduce the low-redshift population of massive, quiescent, spheroid-dominated galaxies, but significantly underpredict the presence of massive quiescent galaxies at $z > 4$. We speculate that either quenching is not effective enough, begins too late, or operates too slowly in these theoretical models.

The results presented in this work thus strongly suggest that our understanding of the physical processes that quench massive galaxies at high redshift is incomplete, and requires further investigation. To have full confidence in this result we must overcome the impact of contamination from dusty low- z interloping galaxies. Observations from ALMA and deep IR imaging and spectroscopy from the *James Webb Space Telescope* (*JWST*) are needed to probe for obscured star formation, and spectroscopically identify the strong 4000 Å break in quiescent galaxies, respectively.

M.L.S. and S.L.F. acknowledge support from the National Science Foundation through grant AST 1614798 and from the NASA Astrophysics and Data Analysis Program through grants NNX16AN46G and 80NSSC18K0954. S.S. S.J. and J.F. gratefully acknowledge support from the University of Texas at Austin, as well as NSF grants AST-1413652, AST-1614798, and AST-1757983. The work of CP and LW is supported by the NSF grant AST 1614668. J.F. acknowledges support from NSF GRFP through the grant DGE-1610403. RSS and LY acknowledge support from the Simons

Foundation and the Downsborough family. We thank the anonymous referee for their constructive comments. We thank Paola Santini, Rachel Bezanson, Justin Spilker, Eric Gawiser, Raquel Martinez, Neal Evans, and Gabe Brammer for useful conversations which improved the quality of this work. We thank Mark Dickinson, David Herrera, Ron Probst, Frank Valdes, and all of the NOAO scientists and staff who helped make this survey possible. We thank Yi-Kuan Chiang, Yaswant Devarakonda, Emily McLinden, Mallory Molina, Sofía Rojas, Heath Shipley, Mimi Song, Vithal Tilvi, Rebecca Tippens, Tim Weinzirl, and Greg Zeimann for volunteering their time to observe with NEWFIRM onsite at Kitt Peak National Observatory.

This work was based on observations at Kitt Peak National Observatory, NSF’s National Optical-Infrared Astronomy Research Laboratory (Prop. ID 13B-0236; PI: S. Finkelstein), which is operated by the Association of Universities for Research in Astronomy (AURA) under cooperative agreement with the National Science Foundation. The authors are honored to be permitted to conduct astronomical research on Iolkam Du’ag (Kitt Peak), a mountain with particular significance to the Tohono O’odham.

PyRAF is a product of the Space Telescope Science Institute, which is operated by AURA for NASA.

Software: Source Extractor (Bertin & Arnouts 1996), PSFEx (Bertin 2011), eazy-py (<https://github.com/gbrammer/eazy-py>), NEWFIRM calibration pipeline (Swaters et al. 2009), pythonFSPS (Foreman-Mackey et al. 2014), Tractor (Lang et al. 2016a,b)

Facilities: Mayall (NEWFIRM), Blanco (DECam), Spitzer (IRAC)

REFERENCES

- Baldry, I. K., Glazebrook, K., Brinkmann, J., et al. 2004, *ApJ*, 600, 681
- Behroozi, P., & Silk, J. 2018, *MNRAS*, 477, 5382
- Bell, E. F., Wolf, C., Meisenheimer, K., et al. 2004, *ApJ*, 608, 752
- Bertin, E. 2011, in *Astronomical Society of the Pacific Conference Series*, Vol. 442, *Astronomical Data Analysis Software and Systems XX*, ed. I. N. Evans, A. Accomazzi, D. J. Mink, & A. H. Rots, 435
- Bertin, E., & Arnouts, S. 1996, *A&AS*, 117, 393
- Brammer, G. B., van Dokkum, P. G., & Coppi, P. 2008, *The Astrophysical Journal*, 686, 1503
- Brammer, G. B., Whitaker, K. E., van Dokkum, P. G., et al. 2009, *ApJL*, 706, L173
- Brennan, R., Choi, E., Somerville, R. S., et al. 2018, *ApJ*, 860, 14
- Brennan, R., Pandya, V., Somerville, R. S., et al. 2015, *MNRAS*, 451, 2933
- Brinchmann, J., Charlot, S., White, S. D. M., et al. 2004, *MNRAS*, 351, 1151
- Bruzual, G., & Charlot, S. 2003, *MNRAS*, 344, 1000
- Cardelli, J. A., Clayton, G. C., & Mathis, J. S. 1989, *Astrophysical Journal*, 345, 245
- Chabrier, G. 2003, *PASP*, 115, 763
- Choi, E., Ostriker, J. P., Naab, T., Oser, L., & Moster, B. P. 2015, *MNRAS*, 449, 4105
- Choi, E., Ostriker, J. P., Naab, T., et al. 2017, *ApJ*, 844, 31
- Conroy, C., & Gunn, J. E. 2010, *ApJ*, 712, 833
- Conroy, C., Gunn, J. E., & White, M. 2009, *ApJ*, 699, 486

- Davé, R., Anglés-Alcázar, D., Narayanan, D., et al. 2019, *MNRAS*, 486, 2827
- Davidzon, I., Ilbert, O., Laigle, C., et al. 2017, *A&A*, 605, A70
- De Lucia, G., & Blaizot, J. 2007, *MNRAS*, 375, 2
- D'Eugenio, C., Daddi, E., Gobat, R., et al. 2020, *ApJL*, 892, L2
- Dunlop, J. S., Cirasuolo, M., & McLure, R. J. 2007, *MNRAS*, 376, 1054
- Finkelstein, S. L., Song, M., Behroozi, P., et al. 2015a, *ArXiv e-prints*, arXiv:1504.00005
- Finkelstein, S. L., Ryan, Russell E., J., Papovich, C., et al. 2015b, *ApJ*, 810, 71
- Florez, J., Jogee, S., Sherman, S., et al. 2020, *MNRAS*, 497, 3273
- Forrest, B., Annunziatella, M., Wilson, G., et al. 2020a, *ApJL*, 890, L1
- Forrest, B., Marsan, Z. C., Annunziatella, M., et al. 2020b, *ApJ*, 903, 47
- Gawiser, E., van Dokkum, P. G., Herrera, D., et al. 2006, *ApJS*, 162, 1
- Geach, J. E., Lin, Y. T., Makler, M., et al. 2017, *The Astrophysical Journal Supplement Series*, 231, 7
- Glazebrook, K., Schreiber, C., Labbé, I., et al. 2017, *Nature*, 544, 71
- Hahn, C., Starkenburg, T. K., Choi, E., et al. 2019, *ApJ*, 872, 160
- Hill, G. J., & HETDEX Consortium. 2016, in *Astronomical Society of the Pacific Conference Series*, Vol. 507, *Multi-Object Spectroscopy in the Next Decade: Big Questions, Large Surveys, and Wide Fields*, ed. I. Skillen, M. Balcells, & S. Trager, 393
- Kauffmann, G., Heckman, T. M., White, S. D. M., et al. 2003, *MNRAS*, 341, 54
- Kimm, T., Somerville, R. S., Yi, S. K., et al. 2009, *MNRAS*, 394, 1131
- Kriek, M., & Conroy, C. 2013, *ApJL*, 775, L16
- Kriek, M., van Dokkum, P. G., Franx, M., et al. 2006, *ApJL*, 649, L71
- Labbé, I., Franx, M., Rudnick, G., et al. 2002, *arXiv.org*, 1107
- Labbé, I., Huang, J., Franx, M., et al. 2005, *ApJL*, 624, L81
- Lang, D., Hogg, D. W., & Mykytyn, D. 2016a, *The Tractor: Probabilistic astronomical source detection and measurement*, *Astrophysics Source Code Library*, , ascl:1604.008
- Lang, D., Hogg, D. W., & Schlegel, D. J. 2016b, *AJ*, 151, 36
- Marchesini, D., Whitaker, K. E., Brammer, G., et al. 2010, *ApJ*, 725, 1277
- Marsan, Z. C., Muzzin, A., Marchesini, D., et al. 2020, *arXiv e-prints*, arXiv:2010.04725
- Martig, M., Bournaud, F., Teyssier, R., & Dekel, A. 2009, *ApJ*, 707, 250
- Mason, C. A., Treu, T., Schmidt, K. B., et al. 2015, *ApJ*, 805, 79
- McCracken, H. J., Milvang-Jensen, B., Dunlop, J., et al. 2012, *A&A*, 544, A156
- Merlin, E., Fontana, A., Castellano, M., et al. 2018, *MNRAS*, 473, 2098
- Merlin, E., Fortuni, F., Torelli, M., et al. 2019, *MNRAS*, 490, 3309
- Muzzin, A., Marchesini, D., Stefanon, M., et al. 2013, *ApJ*, 777, 18
- Nelson, D., Pillepich, A., Springel, V., et al. 2018, *MNRAS*, 475, 624
- Noeske, K. G., Weiner, B. J., Faber, S. M., et al. 2007, *ApJL*, 660, L43
- Oke, J. B., & Gunn, J. E. 1983, *ApJ*, 266, 713
- Pandya, V., Brennan, R., Somerville, R. S., et al. 2017, *MNRAS*, 472, 2054
- Papovich, C., Shipley, H. V., Mehtens, N., et al. 2016, *ApJS*, 224, 28
- Planck Collaboration, Ade, P. A. R., Aghanim, N., et al. 2014, *A&A*, 571, A16
- Probst, R. G., Gaughan, N., Abraham, M., et al. 2004, in *Society of Photo-Optical Instrumentation Engineers (SPIE) Conference Series*, Vol. 5492, *Proc. SPIE*, ed. A. F. M. Moorwood & M. Iye, 1716–1724
- Quadri, R., Marchesini, D., van Dokkum, P., et al. 2007, *AJ*, 134, 1103
- Rodríguez Montero, F., Davé, R., Wild, V., Anglés-Alcázar, D., & Narayanan, D. 2019, *MNRAS*, 490, 2139
- Salmon, B., Papovich, C., Finkelstein, S. L., et al. 2015, *ApJ*, 799, 183
- Santini, P., Merlin, E., Fontana, A., et al. 2019, *MNRAS*, 486, 560
- Schaye, J., Crain, R. A., Bower, R. G., et al. 2014, *ArXiv e-prints*, arXiv:1407.7040
- Schlafly, E. F., & Finkbeiner, D. P. 2011, *The Astrophysical Journal*, 737, 103
- Schreiber, C., Glazebrook, K., Nanayakkara, T., et al. 2018, *A&A*, 618, A85
- Sherman, S., Jogee, S., Florez, J., et al. 2020a, *MNRAS*, 491, 3318
- . 2020b, *MNRAS Submitted*
- Somerville, R. S., & Davé, R. 2015, *ARA&A*, 53, 51

- Somerville, R. S., Hopkins, P. F., Cox, T. J., Robertson, B. E., & Hernquist, L. 2008, *MNRAS*, 391, 481. http://adsabs.harvard.edu/cgi-bin/nph-data_query?bibcode=2008MNRAS.391..481S&link_type=ABSTRACT
- Somerville, R. S., Popping, G., & Trager, S. C. 2015, *MNRAS*, 453, 4337
- Spitler, L. R., Straatman, C. M. S., Labbé, I., et al. 2014, *ApJL*, 787, L36
- Stefanon, M., Marchesini, D., Rudnick, G. H., Brammer, G. B., & Whitaker, K. E. 2013, *ApJ*, 768, 92
- Stefanon, M., Marchesini, D., Muzzin, A., et al. 2015, *ApJ*, 803, 11
- Stevans, M. L., Finkelstein, S. L., Wold, I., et al. 2018, *ApJ*, 863, 63
- Straatman, C. M. S., Labbé, I., Spitler, L. R., et al. 2014, *ApJL*, 783, L14
- Su, K.-Y., Hopkins, P. F., Hayward, C. C., et al. 2019, *MNRAS*, 487, 4393
- Swaters, R. A., Valdes, F., & Dickinson, M. E. 2009, in *Astronomical Society of the Pacific Conference Series*, Vol. 411, *Astronomical Data Analysis Software and Systems XVIII*, ed. D. A. Bohlender, D. Durand, & P. Dowler, 506
- Tacchella, S., Diemer, B., Hernquist, L., et al. 2019, *MNRAS*, 1573
- Tanaka, M., Valentino, F., Toft, S., et al. 2019, *ApJL*, 885, L34
- Valentino, F., Tanaka, M., Davidzon, I., et al. 2020, *ApJ*, 889, 93
- van der Wel, A., Franx, M., van Dokkum, P. G., et al. 2014, *ApJ*, 788, 28
- Weinberger, R., Springel, V., Hernquist, L., et al. 2017, *MNRAS*, 465, 3291
- Weinberger, R., Springel, V., Pakmor, R., et al. 2018, *MNRAS*, 479, 4056
- Wellons, S., Torrey, P., Ma, C.-P., et al. 2015, *MNRAS*, 449, 361
- Whitaker, K. E., Labbé, I., van Dokkum, P. G., et al. 2011, *ApJ*, 735, 86
- Whitaker, K. E., Franx, M., Leja, J., et al. 2014, *ApJ*, 795, 104
- Williams, R. J., Quadri, R. F., Franx, M., et al. 2010, *ApJ*, 713, 738
- Wold, I. G. B., Kawinwanichakij, L., Stevans, M. L., et al. 2019, *ApJS*, 240, 5
- Wuyts, S., Labbé, I., Franx, M., et al. 2007, *ApJ*, 655, 51

APPENDIX

In this appendix, we first list the estimated 50% and 90% K -band completeness for each of the NHS tiles. This was estimated by inputting 2000 mock point-sources in each tile, re-running our photometric measurement process in the same way as in our actual catalog, and calculating the fraction of input sources which were recovered in magnitude bins with $\Delta m=0.05$ mag. The 50% and 90% completeness limits were defined as the faintest bin where the completeness exceeded 50% or 90%, respectively. We note that these completeness limits are applicable to regions of average depth in a given tile. The median completeness limits for the entire survey are: 50% = 22.65 and 90% = 22.15. We first show the completeness curves for all tiles in Figure 14, followed by the 50% and 90% completeness limits in Tables 5–8.

Following the completeness tables, we show summary plots and give a summary table for the nine massive quiescent candidates removed following visual inspection. Finally, In this section we also provide example tables showing the format of the full machine-readable NHS catalog.

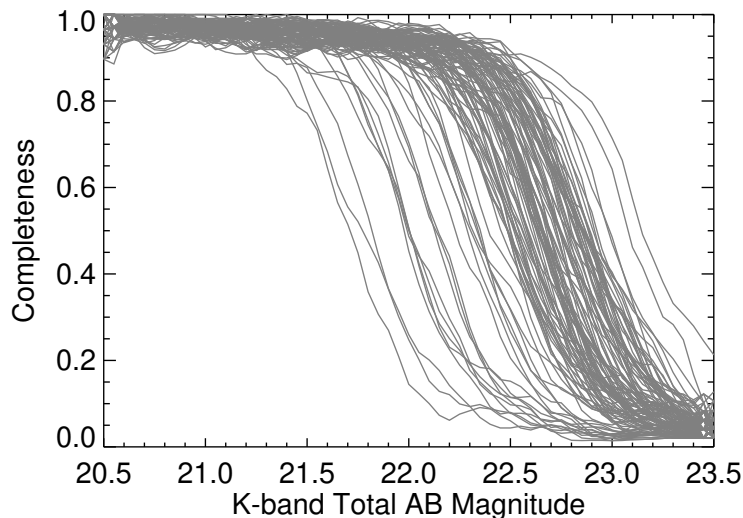


Figure 14. Completeness curves derived from mock-source injection simulations into each tile. The median completeness limits for the entire survey are: 50% = 22.65 and 90% = 22.15.

Table 5. NHS *K*-band Completeness for A Fields

Field	50% Completeness	90% Completeness
A1	22.6	22.2
A2	22.9	22.3
A3	22.8	22.4
A4	22.8	22.4
A5	22.9	22.4
A6	22.9	21.9
A7	22.1	21.8
A8	22.9	22.4
A9	22.6	22.1
A10	22.8	22.4
A11	22.5	22.1
A12	22.5	22.1
A13	22.8	22.4
A14	22.3	21.8
A15	22.7	22.2
A16	22.6	22.2
A17	22.6	22.3
A18	22.9	22.4
A19	21.7	21.2
A20	22.0	21.6
A21	22.2	21.8
A22	22.6	22.2
A23	21.9	21.6
A24	22.9	22.3
A25	22.6	22.2
A26	22.5	21.9
A27	22.4	21.9

Table 6. NHS *K*-band Completeness for B Fields

Field	50% Completeness	90% Completeness
B1	22.6	22.3
B2	22.6	22.1
B3	22.8	22.1
B4	22.7	22.2
B5	22.6	22.1
B6	22.9	22.4
B7	22.9	22.4
B8	22.9	22.4
B9	22.8	22.4
B10	22.7	22.2
B11	22.8	22.4
B12	23.1	22.5
B13	22.8	22.4
B14	22.7	22.2
B15	23.1	22.6
B16	22.9	22.4
B17	22.6	22.3
B18	22.4	22.1
B19	22.6	22.1
B20	22.8	22.2
B21	22.8	22.3
B22	22.6	22.2
B23	22.6	22.2
B24	22.6	22.4
B25	22.9	22.1
B26	22.7	22.4
B27	22.9	22.3
B28	22.6	22.1

Table 7. NHS *K*-band Completeness for C Fields

Field	50% Completeness	90% Completeness
C1	22.9	22.5
C2	22.5	22.1
C3	22.9	22.4
C4	22.9	22.4
C5	22.6	22.2
C6	22.6	22.1
C7	22.7	22.1
C8	22.8	22.4
C9	22.6	22.1
C10	22.6	22.1
C11	22.6	22.1
C12	22.6	22.1
C13	22.0	21.4
C14	22.8	22.3
C15	22.5	22.1
C16	22.6	22.2
C17	22.5	21.9
C18	22.5	22.1
C19	22.7	22.4
C20	22.6	22.3
C21	22.4	21.9
C22	22.8	22.4
C23	22.5	22.0
C24	22.4	22.1
C25	22.7	22.4
C26	22.6	22.2
C27	22.9	22.4
C28	22.8	22.3

Table 8. NHS *K*-band Completeness for D Fields

Field	50% Completeness	90% Completeness
D1	22.4	21.9
D2.3	22.6	22.1
D2.7	22.4	22.0
D2	22.9	22.3
D3	22.1	21.8
D4.3	22.3	21.9
D4.7	22.4	22.0
D4	22.4	21.9
D5	22.4	22.1
D6.3	22.6	22.1
D6.7	22.6	22.1
D6	22.7	22.1
D7	22.3	21.9
D8.3	22.3	21.9
D8.7	22.2	21.9
D8	22.8	22.2
D9	22.6	22.1
D10	22.6	22.2
D10.3	21.8	21.4
D10.7	21.9	21.4
D11	21.8	21.4
D12	22.6	21.9
D13	21.9	21.6
D14	22.6	22.1
D15	22.6	22.2
D16	22.1	21.7

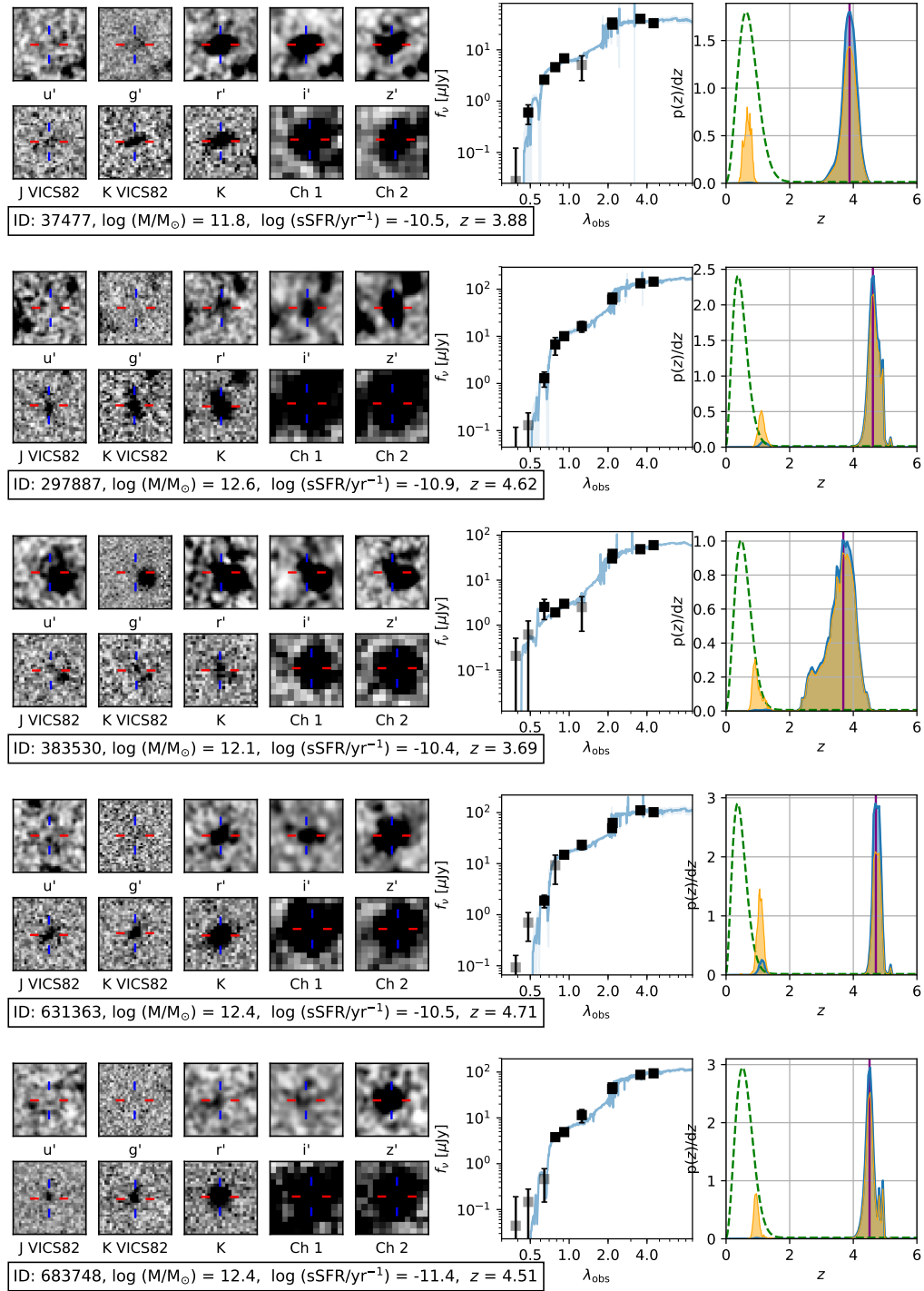


Figure 15. Summary plots of the first five of nine candidate massive quiescent galaxies removed following visual inspection. All symbols are the same as Figure 11

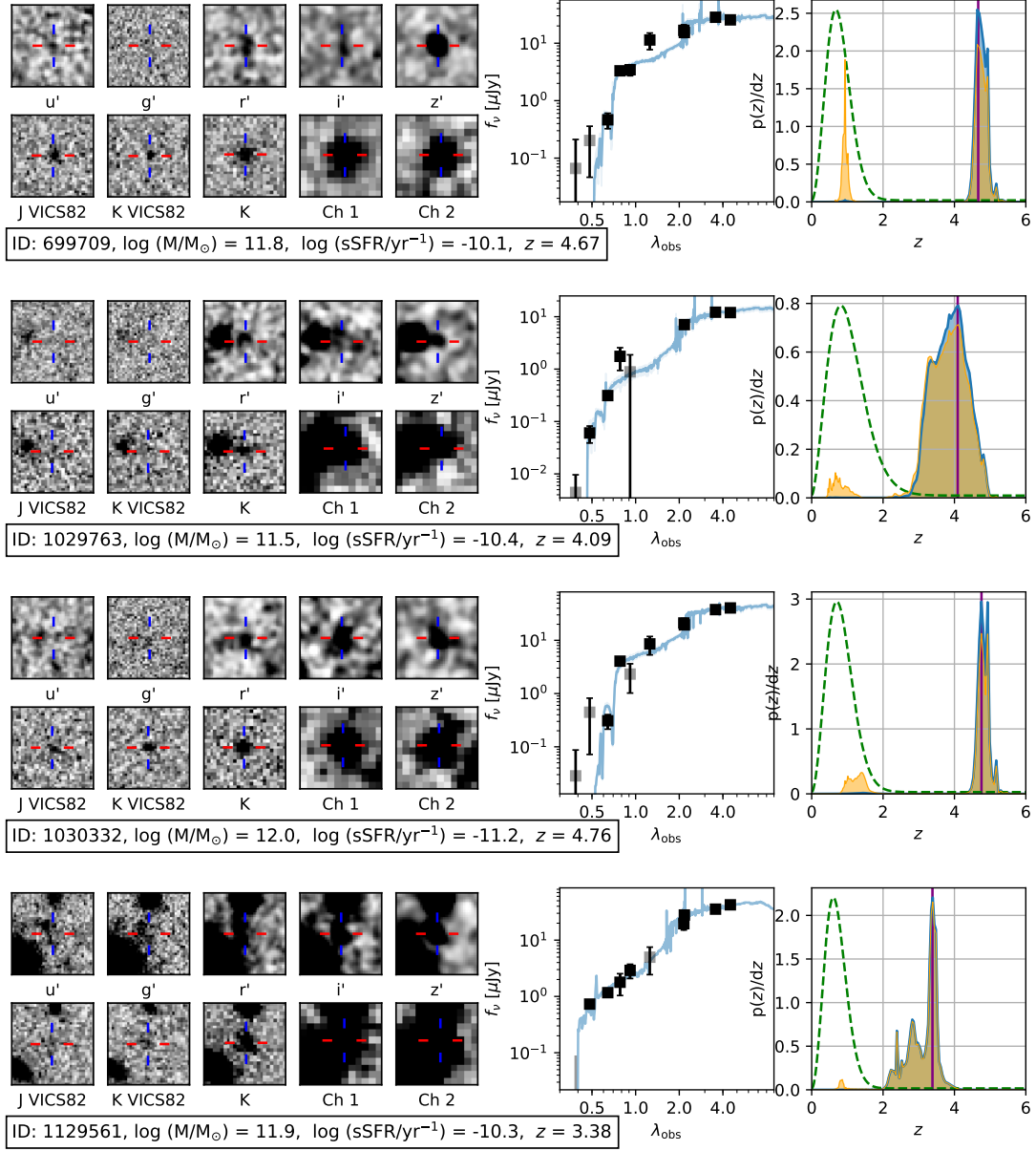


Figure 16. Summary plots of the last four of nine candidate massive quiescent galaxies removed following visual inspection. All symbols are the same as Figure 11

Table 9. Candidate Massive Quiescent Galaxies Removed Following Visual Inspection

ID	RA	Dec	K_{AB}	z_p	$\int P(z_p) > 3$	$\log(M_*)$	$\log(\text{sSFR})$	$\log(M_*)$	$\log \text{sSFR}$	$\int P(\text{sSFR}) < -10.05$
	(J2000)	(J2000)				EAZY	EAZY	BC03	BC03	BC03
	(deg)	(deg)				(M_\odot)	(yr^{-1})	(M_\odot)	(yr^{-1})	
37477 ^s	15.122565	0.086271	20.2	3.88	0.79	11.8	-10.5	11.7	<-11.0	0.79
297887 ^s	16.585555	0.138326	19.3	4.62	0.87	12.6	-10.9	12.5	<-11.8	0.96
383530 ^s	17.528702	0.607760	19.9	3.69	0.80	12.1	-10.4	12.1	-10.4	0.87
631363 ^u	19.715019	0.215609	19.4	4.71	0.68	12.4	-10.5	12.3	<-11.6	0.85
683748 ^s	19.803261	0.133706	19.7	4.51	0.85	12.4	-11.4	12.4	<-11.7	0.98
699709 ^u	19.762647	-0.210499	20.9	4.67	0.82	11.8	-10.1	11.8	<-11.1	0.76
1029763 ^v	22.549563	0.528559	21.8	4.09	0.93	11.5	-10.4	11.5	-10.1	0.89
1030332 ^u	22.401811	0.542126	20.7	4.76	0.83	12.0	-11.2	11.9	<-11.2	0.85
1129561 ^u	23.194968	-0.730294	20.3	3.38	0.63	11.9	-10.3	11.8	-10.1	0.82

NOTE—Properties of the 9 candidate massive quiescent galaxies removed following visual inspection. ^uRemoved due to visible weak flux in the u -band image coincident with the position of the source. ^s Removed due to visibly appearing elongated with measured r_h indicating the source being significantly resolved in the K_s -band imaging ($>1''$). ^vRemoved due to lack of measured VISTA J and K photometry.

Table 10. NHS Catalog Sample

ID	R.A. (J2000)	decl. (J2000)	a	e	θ	$\tau_{1/2}$	$f_{K_s, \text{NHS}}^{\text{AUTO}}$	$\sigma_{K_s, \text{NHS}}^{\text{AUTO}}$	$f_{K_s, \text{NHS}}^{\text{OPT}}$	$\sigma_{K_s, \text{NHS}}^{\text{OPT}}$
(1)	(2)	(3)	(4)	(5)	(6)	(7)	(8)	(9)	(10)	(11)
1100000	23.192657	0.257515	0.0	0.15	34.1	3.3	460.491	1.996	252.966	0.718
1100001	22.954510	0.260587	0.0	0.33	66.7	2.9	18.876	1.079	12.031	0.747
1100002	22.914940	0.261128	0.0	0.08	-1.6	2.1	58.961	0.983	62.439	0.730
1100003	23.125761	0.262926	0.0	0.34	9.0	3.0	5.419	0.456	4.052	0.694
1100004	23.200405	0.262837	0.0	0.43	58.5	1.9	2.616	0.282	2.964	0.711
1100005	22.951833	0.262902	0.0	0.24	53.5	1.9	4.060	0.523	4.840	0.730
1100006	23.151630	0.262835	0.0	0.04	56.1	1.9	3.277	0.424	3.796	0.694
1100007	22.962145	0.262063	0.0	0.24	1.8	2.4	19.283	0.928	17.268	0.745
1100008	23.173936	0.262909	0.0	0.31	-22.2	1.8	4.517	0.554	5.727	0.708
1100009	23.151618	0.260111	0.0	0.13	-35.5	2.8	84.666	1.338	58.754	0.696

NOTE—Table 4 is published in its entirety in the machine-readable format. A portion is shown here for guidance regarding its form and content. (1) Unique object ID number, (2) object R.A. (J2000) in decimal degrees, (3) object decl. (J2000) in decimal degrees, (4) semimajor axis in the detection image, (5) ellipticity measured in the detection image, defined as $e = 1 - b/a$, where b and a are the semiminor and semimajor axes, respectively, (6) position angle measured in the detection image, (7) Source Extractor half-light radius (FLUX_RADIUS), (8) NHS K_s Kron fluxes corrected to total, (9) uncertainties in NHS K_s Kron fluxes corrected to total, (10) NHS K_s optimal-aperture fluxes corrected to total, (11) NHS K_s optimal-aperture fluxes corrected to total, (12, 13, 14, 15) NHS field labels containing source, (16) maximum pixel value in the isophotal area of the source in the data quality mask image, (17, 22, 27, 32, 37) DECam *ugriz* Tractor total fluxes, (18, 23, 28, 33, 38) uncertainties in DECam *ugriz* Tractor total fluxes, (19, 24, 29, 34, 39) DECam *ugriz* Tractor model profiles, (20, 25, 30, 25, 40) DECam *ugriz* Tractor log-probabilities, (21, 26, 31, 36, 41) DECam *ugriz* Tractor flags, (42) JK object ID number from Geach et al. (2017), (43, 45) JK Kron total fluxes from Geach et al. (2017), (44, 46) derived uncertainties in JK Kron total fluxes, (47) Flag for VICS82 sources with values of zero in isophotal area of the source in the WTM, (48, 53) 3.6 and 4.5 μm IRAC Tractor total fluxes, (49, 54) uncertainties in 3.6 and 4.5 μm IRAC Tractor total fluxes, (50, 55) 3.6 and 4.5 μm IRAC Tractor model profiles, (51, 56) 3.6 and 4.5 μm IRAC Tractor log-probabilities, (52, 57) 3.6 and 4.5 μm IRAC Tractor flags, (58) SDSS spectroscopic redshift, (59) *eazy-py* photometric redshift, (60) *eazy-py* photometric redshift χ^2 minimum value, (61) Number of peaks detected in $P(z)$ from *eazy-py*, (62) number of filters used in *eazy-py* photometric redshift estimate, (63) log stellar mass from *eazy-py*, (64) log SFR from *eazy-py*, (65, 66, 67) Rest-frame UVJ magnitudes from *eazy-py*.

Table 10. NHS Catalog Sample (continued)

σ_g	model _g	$\log(P_g)$	Tractor g' Flag	f_r	σ_r	model _r	$\log(P_r)$	Tractor r' Flag	f_i	σ_i	
(μJy)	(24)	(25)	(26)	(μJy)	(27)	(28)	(29)	(30)	(31)	(32)	(33)
1.000	4	-1498032.38	0	84.053	2.769	1	-609655.19	0	135.279	4.470	
0.311	1	-36960160.00	0	7.465	0.739	1	-3387295.75	0	9.377	1.168	
0.102	0	-1453222.62	0	9.256	0.706	4	-179494.30	0	30.529	1.278	
0.090	0	-1360433.12	0	3.711	0.956	4	-205406.78	0	2.718	0.821	
0.207	1	-1342367.88	0	1.008	0.523	1	-173332.89	0	0.452	0.841	
0.442	4	-1842914.88	0	1.165	0.609	1	-441678.34	0	0.265	0.411	
0.207	4	-3033535.00	0	0.830	0.356	1	-6063350.00	0	0.992	0.319	
0.206	0	-1384284.88	0	0.277	0.706	4	-139799.28	0	1.478	0.978	
0.279	4	-1345640.38	0	1.464	0.466	1	-183884.48	0	1.916	0.944	
0.122	4	-1535087.88	0	5.400	0.292	1	-747731.94	0	21.060	2.221	

Table 10. NHS Catalog Sample (continued)

model_i	$\log(P_i)$	Tractor i' Flag	f_z	σ_z	model_z	$\log(P_z)$	Tractor z' Flag	VICS82ID	$f_{\lambda, \text{VICS82}}^{\text{AUTO}}$	$\sigma_{\lambda, \text{VICS82}}^{\text{AUTO}}$
(34)	(35)	(36)	(37)	(38)	(39)	(40)	(41)	(42)	(43)	(44)
			(μJy)	(μJy)				(Geach+17)	(μJy)	(μJy)
1	-419193.06	0	179.684	5.904	1	-318709.12	0	VICS82J013246.24+001527.0	284.44	10.88
1	-822670.38	0	12.094	1.177	1	-192591.42	0	VICS82J013149.10+001538.6	13.89	3.89
1	-188672.66	0	49.241	1.789	1	-128849.97	0	VICS82J013139.59+001540.3	66.51	6.16
1	-166728.31	0	3.377	0.822	1	-122933.82	0	-99	-99.00	-99.00
1	-183598.70	0	2.044	1.239	1	-104748.86	0	-99	-99.00	-99.00
1	-344773.72	0	1.909	1.167	1	-411497.25	0	VICS82J013148.47+001546.7	-99.00	-99.00
1	-4665033.00	0	1.281	0.781	1	-10052148.00	0	VICS82J013236.42+001546.5	-99.00	-99.00
1	-163797.36	0	3.162	1.424	1	-97862.48	0	VICS82J013150.91+001543.5	5.06	2.52
1	-191571.53	0	2.853	0.872	1	-187026.06	0	-99	-99.00	-99.00
4	-423303.53	0	23.014	1.260	1	-638833.19	0	VICS82J013236.40+001536.4	31.67	5.11

Table 10. NHS Catalog Sample (continued)

$f_{K_s}^{\text{AUTO}}$	$\sigma_{K_s}^{\text{AUTO}}$	VICSS82	WTM Flag	$f_{3.6}$	$\sigma_{3.6}$	model _{3,6}	$\log(P_{3,6})$	Tractor 3.6 Flag	$f_{4.5}$	$\sigma_{4.5}$	model _{4,5}	
(μJy)	(μJy)	(46)	(47)	(μJy)	(48)	(49)	(50)	(51)	(52)	(53)	(54)	(55)
463.37	16.42	0	0	257.56	12.76	4	-8.01	0	216.08	10.81	4	
10.07	3.43	0	0	7.82	1.47	0	-2.80	0	8.07	1.57	0	
64.51	6.12	0	0	36.08	2.24	0	-2.51	0	24.17	1.91	0	
-99.00	-99.00	0	0	4.70	1.17	0	-2.15	0	3.50	0.82	1	
-99.00	-99.00	0	0	5.77	1.75	0	-2.05	0	4.60	1.62	0	
9.19	3.30	0	0	8.79	0.85	0	-3.10	0	9.18	0.89	0	
3.02	1.95	0	0	2.95	1.32	0	-19.37	0	2.64	1.45	0	
23.14	4.65	0	0	29.31	2.00	0	-2.72	0	31.09	2.03	0	
-99.00	-99.00	0	0	5.07	1.67	0	-5.73	0	3.00	1.70	0	
68.62	6.21	0	0	96.07	5.08	1	-17.76	0	51.32	3.01	0	

Table 10. NHS Catalog Sample (continued)

$\log(P_{4.5})$	Tractor 4.5 Flag	z_{spec}	z_{phot}	χ^2_{phot}	N_{peaks}	N_{filters}	$\log(M_*)$	$\log(\text{SFR})$	$f_{\text{U,rest}}$	$f_{\text{V,rest}}$	$f_{\text{I,rest}}$
(56)	(57)	(58)	(59)	(60)	(61)	(62)	(63)	(64)	(65)	(66)	(67)
		(SDSS)	(eazy-py)	(eazy-py)	(eazy-py)	(eazy-py)	(M_{\odot})	($M_{\odot} \text{ yr}^{-1}$)	(μJy)	(μJy)	(μJy)
-6.22	0	-99.0000	0.33	1.26	1	10	11.1	0.2	22.3	122.5	378.8
-2.23	0	-99.0000	0.30	4.59	1	10	9.3	-0.4	2.9	8.3	15.6
-2.47	0	-99.0000	0.39	43.61	1	10	10.6	-2.0	2.7	21.6	60.3
-2.14	0	-99.0000	0.64	2.78	2	8	9.1	0.5	2.5	3.5	5.3
-1.88	0	-99.0000	2.58	1.46	2	8	10.2	1.7	1.5	2.4	5.1
-2.54	0	-99.0000	2.46	3.26	1	9	10.5	1.8	1.4	3.3	9.2
-10.77	0	-99.0000	2.09	0.29	6	9	10.2	0.8	1.6	2.9	3.1
-2.22	0	-99.0000	1.30	1.68	2	10	10.8	1.8	1.3	6.5	25.8
-3.45	0	-99.0000	0.74	0.05	3	8	9.3	0.3	1.4	2.1	4.5
-10.75	0	-99.0000	0.63	19.84	1	10	11.1	-1.6	3.1	21.7	75.3